ACCEPTED FOR PUBLICATION IN THE ASTROPHYSICAL JOURNAL
Preprint typeset using LaTeX style emulateapj v. 2/16/10

A PRECISE ASTEROSEISMIC AGE AND RADIUS FOR THE EVOLVED SUN-LIKE STAR KIC 11026764

T. S. METCALFE[1], M. J. P. F. G. MONTEIRO[2], M. J. THOMPSON[3,1], J. MOLENDA-ŻAKOWICZ[4], T. APPOURCHAUX[5], W. J. CHAPLIN[6], G. DOĞAN[7], P. EGGENBERGER[8], T. R. BEDDING[9], H. BRUNTT[10], O. L. CREEVEY[11,12], P.-O. QUIRION[13], D. STELLO[9], A. BONANNO[14], V. SILVA AGUIRRE[15], S. BASU[16], L. ESCH[16], N. GAI[16,17], M. P. DI MAURO[18], A. G. KOSOVICHEV[19], I. N. KITIASHVILI[20], J. C. SUÁREZ[21], A. MOYA[22], L. PIAU[23], R. A. GARCÍA[23], J. P. MARQUES[24], A. FRASCA[14], K. BIAZZO[25], S. G. SOUSA[2], S. DREIZLER[26], M. BAZOT[2], C. KAROFF[6], S. FRANDSEN[7], P. A. WILSON[27,28], T. M. BROWN[29], J. CHRISTENSEN-DALSGAARD[7], R. L. GILLILAND[30], H. KJELDSEN[7], T. L. CAMPANTE[2,7], S. T. FLETCHER[31], R. HANDBERG[7], C. RÉGULO[11,12], D. SALABERT[11,12], J. SCHOU[19], G. A. VERNER[32], J. BALLOT[33], A.-M. BROOMHALL[6], Y. ELSWORTH[6], S. HEKKER[6], D. HUBER[9], S. MATHUR[1], R. NEW[31], I. W. ROXBURGH[32,10], K. H. SATO[23], T. R. WHITE[9], W. J. BORUCKI[34], D. G. KOCH[34], J. M. JENKINS[35]

Draft version September 9, 2010

ABSTRACT

The primary science goal of the *Kepler Mission* is to provide a census of exoplanets in the solar neighborhood, including the identification and characterization of habitable Earth-like planets. The asteroseismic capabilities of the mission are being used to determine precise radii and ages for the target stars from their solar-like oscillations. Chaplin et al. (2010) published observations of three bright G-type stars, which were monitored during the first 33.5 d of science operations. One of these stars, the subgiant KIC 11026764, exhibits a characteristic pattern of oscillation frequencies suggesting that it has evolved significantly. We have derived asteroseismic estimates of the properties of KIC 11026764 from *Kepler* photometry combined with ground-based spectroscopic data. We present the results of detailed modeling for this star, employing a variety of independent codes and analyses that attempt to match the asteroseismic and spectroscopic constraints simultaneously. We determine both the radius and the age of KIC 11026764 with a precision near 1%, and an accuracy near 2% for the radius and 15% for the age. Continued observations of this star promise to reveal additional oscillation frequencies that will further improve the determination of its fundamental properties.

Subject headings: stars: evolution—stars: individual (KIC 11026764)—stars: interiors—stars: oscillations

1. INTRODUCTION

In March 2009 NASA launched the *Kepler* satellite, a mission designed to discover habitable Earth-like planets around distant Sun-like stars. The satellite consists of a 0.95-m telescope with an array of digital cameras that will monitor the brightness of more than 150,000 solar-type stars with a precision of a few parts-per-million for 4-6 years (Borucki et al. 2007). Some of these stars are expected to have planetary systems, and some of the planets will have orbits such that they periodically pass in front of the host star, causing a brief de-

[1] High Altitude Observatory, National Center for Atmospheric Research, Boulder, CO 80307, USA
[2] Centro de Astrofísica and DFA-Faculdade de Ciências, Universidade do Porto, Portugal
[3] School of Mathematics and Statistics, University of Sheffield, Hounsfield Road, Sheffield S3 7RH, UK
[4] Astronomical Institute, University of Wrocław, ul. Kopernika 11, 51-622 Wrocław, Poland
[5] Institut d'Astrophysique Spatiale, Université Paris XI – CNRS (UMR8617), Batiment 121, 91405 Orsay Cedex, France
[6] School of Physics and Astronomy, University of Birmingham, Edgbaston, Birmingham, B15 2TT, UK
[7] Department of Physics and Astronomy, Aarhus University, DK-8000 Aarhus C, Denmark
[8] Geneva Observatory, University of Geneva, Maillettes 51, 1290, Sauverny, Switzerland
[9] Sydney Institute for Astronomy (SIfA), School of Physics, University of Sydney, NSW 2006, Australia
[10] Observatoire de Paris, 5 place Jules Janssen, 92190 Meudon Principal Cedex, France
[11] Instituto de Astrofísica de Canarias, E-38200 La Laguna, Spain
[12] Departamento de Astrofísica, Universidad de La Laguna, E-38206 La Laguna, Spain
[13] Canadian Space Agency, 6767 Boulevard de l'Aéroport, Saint-Hubert, QC, J3Y 8Y9, Canada
[14] INAF – Osservatorio Astrofisico di Catania, Via S.Sofia 78, 95123 Catania, Italy
[15] Max Planck Institute for Astrophysics, Karl Schwarzschild Str. 1, Garching, D-85741, Germany
[16] Department of Astronomy, Yale University, P.O. Box 208101, New Haven, CT 06520-8101, USA
[17] Beijing Normal University, Beijing 100875, P.R. China
[18] INAF-IASF Roma, Istituto di Astrofisica Spaziale e Fisica Cosmica, via del Fosso del Cavaliere 100, 00133 Roma, Italy
[19] HEPL, Stanford University, Stanford, CA 94305-4085, USA
[20] Center for Turbulence Research, Stanford University, 488 Escondido Mall, Stanford, CA 94305, USA
[21] Instituto de Astrofísica de Andalucía (CSIC), CP3004, Granada, Spain
[22] Laboratorio de Astrofísica, CAB (CSIC-INTA), Villanueva de la Cañada, Madrid, PO BOX 78, 28691, Spain
[23] Laboratoire AIM, CEA/DSM-CNRS, Université Paris 7 Diderot, IRFU/SAp, Centre de Saclay, 91191, Gif-sur-Yvette, France
[24] LESIA, CNRS UMR 8109, Observatoire de Paris, Université Paris 6, Université Paris 7, 92195 Meudon Cedex, France
[25] Arcetri Astrophysical Observatory, Largo Enrico Fermi 5, 50125 Firenze, Italy
[26] Georg-August Universität, Institut für Astrophysik, Friedrich-Hund-Platz 1, D-37077 Göttingen
[27] Nordic Optical Telescope, Apartado 474, E-38700 Santa Cruz de La Palma, Santa Cruz de Tenerife, Spain
[28] Institute of Theoretical Astrophysics, University of Oslo, P.O. Box 1029, Blindern, N-0315 Oslo, Norway
[29] Las Cumbres Observatory Global Telescope, Goleta, CA 93117, USA
[30] Space Telescope Science Institute, Baltimore, MD 21218, USA
[31] Materials Engineering Research Institute, Sheffield Hallam University, Sheffield, S1 1WB, UK
[32] Astronomy Unit, Queen Mary, University of London, Mile End Road, London, E1 4NS, UK
[33] Laboratoire d'Astrophysique de Toulouse-Tarbes, Université de Toulouse, CNRS, 14 av E. Belin, 31400 Toulouse, France
[34] NASA Ames Research Center, MS 244-30, Moffett Field, CA 94035, USA
[35] SETI Institute, NASA Ames Research Center, MS 244-30, Moffett Field, CA 94035, USA

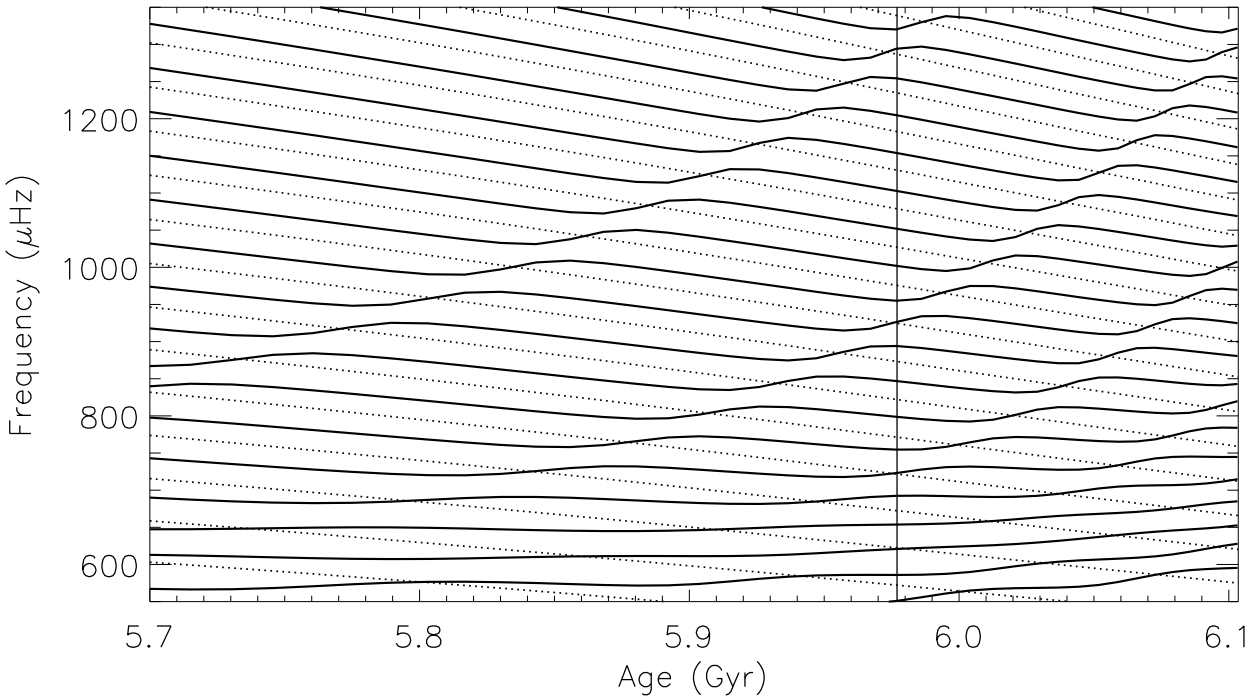

Figure 1. Evolution of the $l = 0$ (dotted) and $l = 1$ (solid) oscillation frequencies as a function of age for a representative stellar model of KIC 11026764. The frequency separation between consecutive $l = 1$ modes during an avoided crossing is a strong function of the stellar age. Note the prediction of a high-frequency avoided crossing above 1250 μHz for Model AA, indicated by the vertical line.

crease in the amount of light recorded by the satellite. The depth of such a *transit* contains information about the size of the planet relative to the size of the host star.

Since we do not generally know the precise size of the host star, the mission design includes a revolving selection of 512 stars monitored with the higher cadence that is necessary to detect short period solar-like oscillations, allowing us to apply the techniques of asteroseismology (Christensen-Dalsgaard et al. 2007; Aerts et al. 2010). Even a relatively crude analysis of such measurements can lead to reliable determinations of stellar radii to help characterize the extra-solar planetary systems discovered by the mission, and stellar ages to reveal how such systems evolve over time. For the asteroseismic targets that do not contain planetary companions, these data will allow a uniform determination of the physical properties of hundreds of solar-type stars, providing a new window on stellar structure and evolution.

Initial results from the Kepler Asteroseismic Investigation were presented by Gilliland et al. (2010a), while a more detailed analysis of the solar-like oscillations detected in several early targets was published by Chaplin et al. (2010). The latter paper includes observations of three bright (V$\sim$9) G-type stars, which were monitored during the first 33.5 d of science operations. One of these stars, the subgiant KIC 11026764 ($\equiv$ 2MASS J19212465+4830532 $\equiv$ BD+48 2882 $\equiv$ TYC 3547-12-1), exhibits a characteristic pattern of oscillation frequencies suggesting that it has evolved significantly.

In unevolved stars, the high radial order (n) acoustic oscillation modes (p-modes) with a given spherical degree (l) are almost evenly spaced in frequency. As the star evolves and the envelope expands, the p-mode frequencies gradually decrease. Meanwhile, as the star becomes more centrally condensed, the buoyancy-driven (g-mode) oscillations in the core shift to higher frequencies. This eventually leads to a range of frequencies where the nonradial ($l > 0$) oscillation modes can take on a mixed character, behaving like g-modes in the core and p-modes in the envelope ("mixed modes"), with their frequencies shifted as they undergo so-called *avoided crossings* (Osaki 1975; Aizenman et al. 1977). This behavior changes relatively quickly with stellar age, and propagates from one radial order to the next as the star continues to evolve (see Figure 1). Consequently, those modes that deviate significantly from uniform frequency spacing yield a strong (though model-dependent) constraint on the age of the star (e.g., see Christensen-Dalsgaard 2004). Avoided crossings have been observed in the subgiant stars η Boo (Kjeldsen et al. 1995, 2003; Carrier et al. 2005) and β Hyi (Bedding et al. 2007), and possibly also in Procyon (Bedding et al. 2010) and HD 49385 (Deheuvels et al. 2010). As noted by Gilliland et al. (2010a) and Chaplin et al. (2010) the dipole ($l = 1$) modes observed in KIC 11026764 show the signature of an avoided crossing, raising the exciting possibility that detailed modeling of this star will provide a very precise determination of its age.

In this paper we derive the stellar age, radius and other characteristics of KIC 11026764 by matching both the observed oscillation frequencies from *Kepler* photometry and the best available spectroscopic constraints from ground-based observations. We describe the extraction and identification of the oscillation frequencies in §2, and the analysis of ground-based data for spectroscopic constraints in §3. In §4 we provide the details of the independent codes and analysis methods used for the fitting, and in §5 we describe our final modeling results. We summarize and discuss the broader significance of the results in §6.

2. OSCILLATION FREQUENCIES

The 58.85-second (short-cadence) photometric data on KIC 11026764 came from the first 33.5 d of science operations (2009 May 12 to June 14). Time series data were then

Table 1
The minimal and maximal sets of observed oscillation frequencies for KIC 11026764.

	Minimal Frequency Set (μHz)			Maximal Frequency Set (μHz)		
n^*	$l=0$	$l=1$	$l=2$	$l=0$	$l=1$	$l=2$
10	...	...	...	...	...	615.49 ± 0.45[b]
11	620.79 ± 0.29[c]	653.80 ± 0.23	...	620.42 ± 0.37[c]	654.16 ± 0.39	670.23 ± 1.21[a]
12	...	...	...	673.97 ± 0.71[a]	699.87 ± 0.66[b]	716.36 ± 0.21[b]
13	723.63 ± 0.10	755.28 ± 0.26	767.46 ± 0.46	723.30 ± 0.24	754.85 ± 0.23	769.16 ± 0.71
14	772.82 ± 0.30	799.96 ± 0.40	817.91 ± 0.58	772.53 ± 0.33	799.72 ± 0.23	818.81 ± 0.30
15	822.72 ± 0.14	847.57 ± 0.30	867.66 ± 0.86	822.46 ± 0.31	846.88 ± 0.34	868.31 ± 0.24
16	873.55 ± 0.14	893.48 ± 0.33	...	873.30 ± 0.27	893.52 ± 0.20	919.31 ± 0.52[a]
17	924.53 ± 0.37	953.57 ± 0.39	969.77 ± 0.36	924.10 ± 0.29	953.51 ± 0.22	970.12 ± 0.68
18	974.59 ± 0.35	1000.41 ± 0.52	1020.72 ± 1.33	974.36 ± 0.26	1000.38 ± 0.41	1019.72 ± 0.44
19	1025.48 ± 0.63	1049.99 ± 0.35	...	1025.16 ± 0.37	1049.34 ± 0.29	1072.49 ± 0.62[a]
20	1076.70 ± 0.29	...	...	1076.52 ± 0.51	...	...

[*] Reference value of n, not used for model-fitting. [a] Observed mode adopted for refined model-fitting.
[b] Mode not present in any of the optimal models. [c] Models suggest an alternate mode identification (see §6).

prepared from the raw observations in the manner described by Gilliland et al. (2010b). The power spectrum is shown in Figures 1 and 2 of Chaplin et al. (2010). Eight teams extracted estimates of the mode frequencies of the star. The teams used slightly different strategies to extract those estimates, but the main idea was to maximize the likelihood (Anderson et al. 1990) of a multi-parameter model designed to describe the frequency-power spectrum of the time series. The model included Lorentzian peaks to describe the p-modes, with flat and power-law terms in frequency (e.g., Harvey 1985) to describe instrumental and stellar background noise.

The fitting strategies followed well-established recipes. Some teams performed a global fit—optimizing simultaneously every free parameter needed to describe the observed spectrum (e.g., see Appourchaux et al. 2008)—while others fit the spectrum a few modes at a time, an approach traditionally adopted for Sun-as-a-star data (e.g., see Chaplin et al. 1999). Some teams also incorporated a Bayesian approach, with the inclusion of priors in the optimization and Markov Chain Monte Carlo (MCMC) analysis to map the posterior distributions of the estimated frequencies (e.g., see Benomar et al. 2009; Campante et al. 2010).

We then implemented a procedure to select two of the eight sets of frequencies, which would subsequently be passed to the modeling teams. Use of individual sets—as opposed to some average frequency set—meant that the modeling could rely on an easily reproducible set of input frequencies, which would not be the case for an average set. We selected a *minimal frequency* set to represent the modes that all teams agreed upon within the errors, and a *maximal frequency* set, which included all possible frequencies identified by at least two of the teams, as explained below.

From the sets of frequencies $\nu_{nl,i}$ provided by the eight teams, we calculated a list of average frequencies $\bar{\nu}_{nl}$. For each mode $\{n,l\}$, we computed the number of teams returning frequencies that satisfied

$$|\nu_{nl,i} - \bar{\nu}_{nl}| \leq \sigma_{nl,i}, \quad (1)$$

with $\sigma_{nl,i}$ representing the frequency uncertainties returned by each team. We then compiled a *minimal* list of modes. For each $\{n,l\}$ we counted the total number of teams with identified frequencies, as well as the number of those frequencies that satisfied Eq.(1). Modes for which *all* identifications satisfied the inequality were added to the minimal list. We also compiled a *maximal* list of modes, subject to the much more relaxed criterion that the $\{n,l\}$ satisfying Eq.(1) should be identified by at least two teams.

In the final stage of the procedure, we computed for each of the eight frequency sets the normalized root-mean-square (*rms*) deviations with respect to the $\bar{\nu}_{nl}$ of the minimal and maximal lists of modes. The frequency set with the smallest *rms* deviation with respect to the minimal list was chosen to be the *minimal frequency* set, while the set with the smallest *rms* deviation with respect to the maximal list was chosen to be the *maximal frequency* set. The minimal frequency set was also used by Chaplin et al. (2010), and provided the initial constraints for the modeling teams (see Table 1). The maximal frequency set was used later for additional validation, as explained in §5. Note that the same modes have slightly different frequencies in these two sets, since they come from individual analyses. The true radial order (n) of the modes can only be determined from a stellar model, so we provide arbitrary reference values for convenience.

3. GROUND-BASED DATA

KIC 11026764 (α_{2000} = 19$^{\rm h}$21$^{\rm m}$24$^{\rm s}$.65, δ_{2000} = +48°30′53.″2) has a magnitude of V = 9.55. The atmospheric parameters given in the Kepler Input Catalog[36] (KIC; Latham et al. 2005) as derived from photometric observations acquired in the Sloan filters are $T_{\rm eff}$ = 5502 K, $\log g$ = 3.896 dex, and [Fe/H] = –0.255 dex. The quoted uncertainties on these values are 200 K in $T_{\rm eff}$ and 0.5 dex in $\log g$ and [Fe/H]. Since this level of precision is minimally useful for asteroseismic modeling, we acquired a high-resolution spectrum of the star to derive more accurate values of its effective temperature, surface gravity, and metallicity.

3.1. *Observations and Data Reduction*

The spectrum was acquired with the Fibre-fed Echelle Spectrograph (FIES) at the 2.56-m Nordic Optical Telescope

[36] http://archive.stsci.edu/kepler/kepler_fov/search.php

(NOT) on 2009 November 9 (HJD 2455145.3428). The 1800 s exposure covers the wavelength range 3730-7360 Å at a resolution R∼67000 and signal-to-noise ratio S/N = 80 at 4400 Å. The Th-Ar reference spectrum was acquired immediately after the stellar spectrum. The reduction was performed with the FIESTOOL software, which was developed specifically for the FIES instrument and performs all of the conventional steps of echelle data reduction[37]. This includes the subtraction of bias frames, modeling and subtraction of scattered light, flat-field correction, extraction of the orders, normalization of the spectra (including fringe correction), and wavelength calibration.

3.2. *Atmospheric Parameters*

We derived the atmospheric parameters of KIC 11026764 using several methods to provide an estimate of the external errors on $T_{\rm eff}$, $\log g$, and [Fe/H], which would be used in the asteroseismic modeling. The five independent reductions included: the VWA[38] software package (Bruntt et al. 2004, 2010a), the MOOG[39] code (Sneden 1973), the ARES[40] code (Sousa et al. 2007), the SYNSPEC method (Hubeny 1988; Hubeny & Lanz 1995), and the ROTFIT code (Frasca et al. 2003, 2006). The principal characteristics of the methods employed by each of these codes are described below, and the individual results are listed in Table 2.

For the VWA method, the $T_{\rm eff}$, $\log g$ and microturbulence of the adopted MARCS atmospheric models (Gustafsson et al. 2008) are adjusted to minimize the correlations of Fe I with line strength and excitation potential. The atmospheric parameters are then adjusted to ensure agreement between the mean abundances of Fe I and Fe II. Additional constraints on the surface gravity come from the two wide Ca lines at 6122 and 6162 Å, and from the Mg-1b lines (Bruntt et al. 2010b). The final value of $\log g$ is the weighted mean of the results obtained from these methods. The mean metallicity is calculated only from those elements (Si, Ti, Fe and Ni) exhibiting at least 10 lines in the observed spectrum. The uncertainties in the derived atmospheric parameters are determined by perturbing the computed models, as described in Bruntt et al. (2008). Having computed the mean atmospheric parameters for the star, VWA finally determines abundances for all of the elements contained in the spectrum (see Figure 2). No trace of Li I 6707.8 absorption is seen in the spectrum of KIC 11026764. We estimate an upper limit for the equivalent width EW $\leq$ 5 mÅ.

The 2002 version of the MOOG code determines the iron abundance under the assumption of local thermodynamic equilibrium (LTE), using a grid of 1D model atmospheres by Kurucz (1993). The LTE iron abundance was derived from the equivalent widths of 65 Fe I and 10 Fe II lines in the 4830-6810 Å range, measured with a Gaussian fitting procedure in the IRAF[41] task *splot*. For the analysis, we followed the prescription of Randich et al. (2006), using the same list of lines as Biazzo et al. (2010). The effective temperature and microturbulent velocity were determined by requiring that the iron abundance be independent of the excitation potentials and the equivalent widths of Fe I lines. The surface gravity was determined by requiring ionization equilibrium between Fe I and Fe II. The initial values for the effective temperature, surface gravity, and microturbulence were chosen to be solar ($T_{\rm eff}$ = 5770 K, $\log g$ = 4.44 dex, and ξ = 1.1 km s^{-1}).

ARES provides an automated measurement of the equivalent widths of absorption lines in stellar spectra: the LTE abundance is determined differentially relative to the Sun with the help of MOOG and a grid of ATLAS-9 plane-parallel model atmospheres (Kurucz 1993). We used ARES with two different lists of iron lines: a 'short' one composed of isolated iron lines (Sousa et al. 2006), and a 'long' one composed of iron lines suitable for automatic measurements (Sousa et al. 2008). Our computations resulted in two consistent sets of atmospheric parameters for KIC 11026764.

SYNSPEC provides synthetic spectra based on model atmospheres, either calculated by TLUSTY or taken from the literature. We used the new grid of ATLAS-9 models (Kurucz 1993; Castelli & Kurucz 2003) to calculate synthetic spectra, which were then compared to the observed spectrum. Based on the list of iron lines from Sousa et al. (2008), we derived the stellar parameters in two ways to estimate the uncertainty due to the normalization of the observed spectrum. For the first approach we determined the minimum χ^2 of the deviation between the synthetic iron lines and the observed spectrum for a fixed set of stellar parameters. For the second approach, we determined the best fitting effective temperature and surface gravity for each iron line from the list, and adopted stellar parameters from the mean. The primary uncertainty in the final parameters arises from the correlation between the effective temperature and surface gravity: a reduction of the effective temperature can be compensated by a reduction of the gravity. While the χ^2 method results in lower values for both parameters ($T_{\rm eff}$ = 5560 K, $\log g$ = 3.62 dex), the averaging approach yields higher values ($T_{\rm eff}$ = 5701 K, $\log g$ = 3.95 dex). The differences between the two results exceed the formal errors of each method. We therefore adopt the mean, and assume half of the difference for the uncertainty. The metallicity is determined by minimizing the scatter in the parameters derived from individual lines.

ROTFIT performs a simultaneous and fast determination of $T_{\rm eff}$, $\log g$, and [Fe/H] for a star—as well as its projected rotational velocity $v \sin i$—by comparing the observed spectrum with a library of spectra for reference stars (see Katz et al. 1998; Soubiran et al. 1998). The adopted estimates for the stellar parameters come from a weighted mean of the pa-

Table 2
Atmospheric parameter estimates for KIC 11026764.

$T_{\rm eff}$	$\log g$	[Fe/H]	Method
5640 ± 80	3.84 ± 0.10	$+0.02 \pm 0.06$	VWA
5750 ± 50	4.10 ± 0.10	$+0.11 \pm 0.06$	MOOG
5774 ± 39	4.01 ± 0.07	$+0.09 \pm 0.03$	ARES[a]
5793 ± 26	4.06 ± 0.04	$+0.10 \pm 0.02$	ARES[b]
5630 ± 70	3.79 ± 0.17	$+0.10 \pm 0.07$	SYNSPEC
5777 ± 77	4.19 ± 0.16	$+0.07 \pm 0.08$	ROTFIT

[a] 40 Fe I and 12 Fe II lines from Sousa et al. (2006).
[b] 247 Fe I and 34 Fe II lines from Sousa et al. (2008).

[37] http://www.not.iac.es/instruments/fies/fiestool/FIEStool.html
[38] http://www.hans.bruntt.dk/vwa/
[39] http://verdi.as.utexas.edu/
[40] http://www.astro.up.pt/∼sousasag/ares/
[41] IRAF is distributed by the National Optical Astronomy Observatories, which are operated by the Association of Universities for Research in Astronomy, Inc., under cooperative agreement with the National Science Foundation.

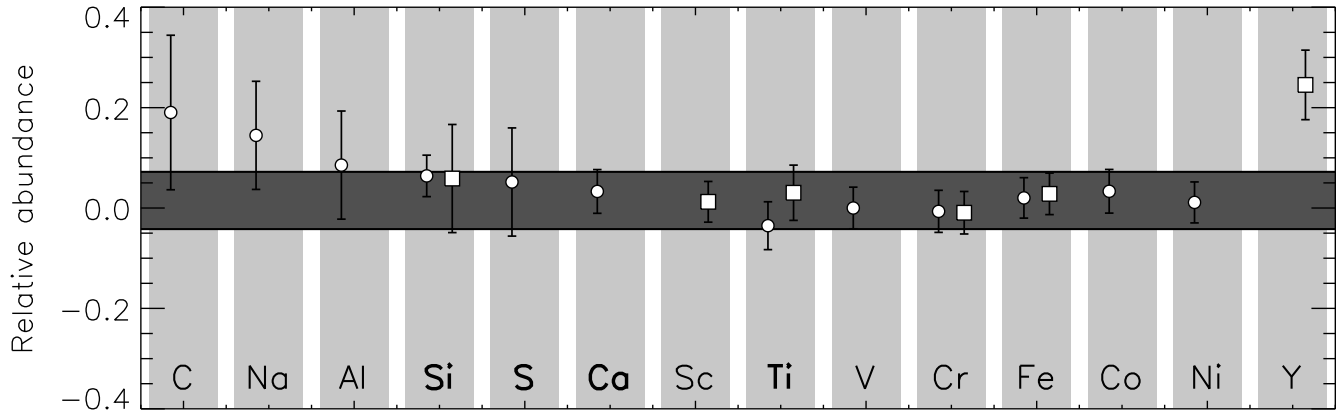

Figure 2. The mean abundances of the elements in the spectrum of KIC 11026764 as derived with the VWA software, including neutral lines (circles) and singly ionized lines (squares). The species labeled in bold are alpha elements. The horizontal bar indicates the mean metallicity of the star and the 1σ uncertainty range of the determination. The abundances are given relative to solar (Grevesse at al. 2007).

rameters for the 10 reference stars that most closely resemble the target spectrum, which is quantified by a χ^2 measure. We applied the ROTFIT code to all echelle orders between 21-69, which cover the range 4320-6770 Å in the observed spectrum. We also derived a projected rotational velocity for KIC 11026764 of 2.8 ± 1.6 km s^{-1}.

3.3. *Adopted Spectroscopic Constraints*

The effective temperature of KIC 11026764 derived from the five methods outlined above generally have overlapping 1σ errors. They all point to a star that is hotter than the KIC estimate by 100-300 K. We find reasonable agreement between the derived values for surface gravity and the KIC estimate. Most of the applied methods result in $\log g$ above 4.0 dex, again slightly higher than in the KIC. Only VWA and SYNSPEC yield slightly lower values, which is not surprising considering the correlation between $T_{\rm eff}$ and $\log g$. Finally, all of the methods agree that the star is slightly metal-rich compared to the Sun, in contrast to the photometric estimate of [Fe/H] = –0.255 dex from the KIC. The initial set of spectroscopic constraints provided to the modeling teams (see §4) came from a mean of the preliminary results from the analyses discussed above, with uncertainties large enough to cover the full range for each parameter: $T_{\rm eff} = 5635 \pm 185$ K, $\log g = 3.95 \pm 0.25$ dex, and [Fe/H] = -0.06 ± 0.25 dex.

For the final estimate of the atmospheric parameters (see §5) we adopted the results from the VWA method, since it has been carefully tested against direct methods for 10 nearby solar-type stars. Specifically, Bruntt et al. (2010a) used VWA to determine $T_{\rm eff}$ from high-quality spectra and these values were compared to a direct method (nearly independent of model atmospheres) using the measured angular diameters from interferometry and bolometric flux measurements. A comparison of the direct (interferometric) and indirect (VWA) methods showed only a slight offset of -40 ± 20 K, and this offset has been removed for KIC 11026764. Similarly, Bruntt et al. (2010a) determined the spectroscopic $\log g$ parameter, which agrees very well for the three binary stars in their sample where the absolute masses and radii (and hence $\log g$) have been measured. Based on these comparisons of direct and indirect methods, Bruntt et al. (2010a) also discuss the issue of realistic uncertainties on spectroscopic parameters, and their estimates of the systematic uncertainties have been incorporated into the adopted values from VWA listed in Table 2.

4. STELLAR MODEL SEARCH

Starting with the minimal frequency set described in §2 and the initial set of spectroscopic constraints from §3, eleven teams of modelers performed a "meta-search" of the parameter space. Each modeler had complete freedom to decide on the input physics and fitting strategy to optimize the match to the observations. The results of the individual fits were evaluated in a uniform manner and ranked according to the total χ^2 between the observed and calculated values of the individual oscillation frequencies and the spectroscopic properties. These individual fits are listed in Table 3, and the details of the codes and fitting strategies employed by each team of modelers are described in the following subsections.

4.1. *Model A*

We employed the Aarhus stellar evolution code (ASTEC; Christensen-Dalsgaard 2008a) for stellar evolution computations, and the adiabatic pulsation package (ADIPLS; Christensen-Dalsgaard 2008b) for frequency calculations. The input physics for the evolution calculations included the OPAL 2005 equation of state (Rogers & Nayfonov 2002), OPAL opacity tables (Iglesias & Rogers 1996) with low-temperature opacities from Ferguson et al. (2005), and the NACRE nuclear reaction rates (Angulo et al. 1999). Convection was treated according to the mixing-length theory of Böhm-Vitense (1958). We did not include diffusion or convective overshoot in the models.

We computed several grids of evolutionary tracks spanning the parameter space around the values given by Chaplin et al. (2010). We primarily adjusted the stellar mass and metallicity in our grids, while fixing the mixing-length parameter α to 1.7. We scanned the parameter space in mass M from 1.00 to 1.35 $M_\odot$; initial heavy-element mass fraction $Z_{\rm i}$ from 0.009 to 0.025; and initial hydrogen mass fraction $X_{\rm i}$ from 0.68 to 0.76. These values of $Z_{\rm i}$ and $X_{\rm i}$ cover a range of $(Z/X)_{\rm i}$ = 0.012-0.037, or [Fe/H] = –0.317 to +0.177 dex using [Fe/H] = $\log(Z/X) - \log(Z/X)_\odot$, where (Z/X) is the ratio at the stellar surface and $(Z/X)_\odot$ = 0.0245 (Grevesse & Noels 1993). This range of [Fe/H] is compatible with the initial spectroscopic constraints. However, we later extended our grids to determine whether there was a better model with lower or higher metallicity. For all of the models on our tracks, we calculated the oscillation frequencies when the values of $T_{\rm eff}$ and $\log g$ were within 2σ of the derived values (see

Table 3
Initial model-fitting search for KIC 11026764.

Model	$M/M_\odot$	Z_s	Y_s	α	t (Gyr)	$L/L_\odot$	$R/R_\odot$	$T_{\rm eff}$(K)	$\log g$	[Fe/H]	χ^2
A	1.13	0.019	0.291	1.70	5.967	3.523	2.026	5562	3.878	+0.051	9.8
B	1.23	0.015	0.250	1.80	4.861	4.730	2.097	5885	3.885	–0.068	12.4
C	1.24	0.021	0.275	1.79	5.231	4.293	2.093	5750	3.890	+0.120	22.5
D	1.31	0.044	0.241	1.42	7.775	2.598	2.139	5016	3.895	+0.400	49.7
E	1.22	0.013	0.233	1.83	4.745	4.710	2.080	5899	3.888	–0.100	55.8
F	1.10	0.014	0.269	1.85	5.839	3.850	2.015	5706	3.870	–0.102	60.6
G	1.20	0.022	0.291	1.88	5.100	3.960	2.160	5663	3.880	+0.116	66.8
H	1.10	0.010	0.250	1.75	6.752	3.776	2.012	5677	3.872	–0.250	284.3
I	1.27	0.021	0.280	0.50	3.206	3.202	1.792	4854	4.034	+0.080	637.3
J	1.12	0.016	0.276	1.90	6.505	3.644	2.026	5593	3.870	–0.139	···
±error	0.14	0.007	0.030	0.78	1.961	0.678	0.091	188	0.023	±0.166	···
K	1.13	0.017	0.283	1.80	6.450	3.610	1.988	5634	3.890	–0.044	···
±error	0.13	0.009	0.009	···	1.930	0.770	0.080	161	0.018	±0.250	···

§3.3). We then assigned a goodness of fit to the frequency set of each model by calculating χ^2:

$$\chi^2 = \frac{1}{N}\sum_{n,l}\left(\frac{\nu_l^{\rm obs}(n)-\nu_l^{\rm model}(n)}{\sigma(\nu_l^{\rm obs}(n))}\right)^2, \quad (2)$$

where N is the total number of modes included, $\nu_l^{\rm obs}(n)$ and $\nu_l^{\rm model}(n)$ are the observed and model frequencies for a given spherical degree l and radial order n, while $\sigma(\nu_l^{\rm obs}(n))$ represents the uncertainties on the observed frequencies. We calculated χ^2 after correcting the frequencies for surface effects, following Kjeldsen et al. (2008):

$$\nu_{\rm obs}(n)-\nu_{\rm best}(n) = a\left[\frac{\nu_{\rm obs}(n)}{\nu_0}\right]^b, \quad (3)$$

where $\nu_{\rm obs}(n)$ and $\nu_{\rm best}(n)$ are the observed and best model frequencies with spherical degree $l = 0$ and radial order n, and ν_0 is the frequency of maximum power in the oscillation spectrum, which is 857μHz for KIC 11026764. We fixed the exponent b to the value derived for the Sun ($b = 4.90$) by Kjeldsen et al. (2008), and a was calculated for each model. We computed smaller and more finely sampled grids around the models with the lowest χ^2 to refine the fit. The properties of the best model are listed in Table 3. Although we found models with higher or lower $\log g$ that had large separations quite close to the observed value, the individual frequencies were not close to the observations, and the larger range of metallicity did not yield improved results. We also found more massive models (around 1.3 $M_\odot$) with a total χ^2 value comparable to our best fit, but they did not include the mixed modes. Model A is the best match from the family of solutions (also including Models F, H, J and K) with masses near 1.1 $M_\odot$.

4.2. *Model B*

We used the Geneva stellar evolution code including rotation (Eggenberger et al. 2008) for all computations. This code includes the OPAL equation of state (Rogers & Nayfonov 2002), the OPAL opacities (Iglesias & Rogers 1996) complemented at low temperatures with the molecular opacities of Alexander & Ferguson (1994), the NACRE nuclear reaction rates (Angulo et al. 1999) and the standard mixing-length formalism for convection (Böhm-Vitense 1958). Overshooting from the convective core into the surrounding radiatively stable layers by a distance $d_{\rm ov} \equiv \alpha_{\rm ov}\min[H_p, r_{\rm core}]$ (Maeder & Meynet 1989) is included with an overshoot parameter $\alpha_{\rm ov} = 0.1$.

In the Geneva code, rotational effects are computed in the framework of shellular rotation. The transport of angular momentum then obeys an advection-diffusion equation (Zahn 1992; Maeder & Zahn 1998), while the vertical transport of chemicals through the combined action of vertical advection and strong horizontal diffusion can be described as a purely diffusive process (Chaboyer & Zahn 1992). Since the modeling of these rotational effects has been described in previous papers (e.g. Eggenberger et al. 2010), we simply note that the Geneva code includes a comprehensive treatment of shellular rotation and that meridional circulation is treated as a truly advective process. For a detailed analysis of the effect of centrifugal force on the oscillation frequencies, see Appendix A. In addition to rotation, atomic diffusion of helium and heavy elements is included with diffusion coefficients calculated according to the prescription of Paquette et al. (1986).

The properties of a stellar model including rotation depend on six parameters: the mass M, the age t, the mixing-length parameter $\alpha \equiv l/H_p$ for convection, the initial rotation velocity on the ZAMS and two parameters describing the initial chemical composition of the star. For these two parameters, we chose the initial helium abundance $Y_{\rm i}$ and the initial ratio between the mass fraction of heavy elements and hydrogen $(Z/X)_{\rm i}$. This ratio can be related to the metallicity [Fe/H] assuming that $\log(Z/X) \cong {\rm [Fe/H]} + \log(Z/X)_\odot$; we adopt the solar value $(Z/X)_\odot = 0.0245$ given by Grevesse & Noels (1993). For these computations, the mixing-length parameter was fixed to a solar calibrated value ($\alpha_\odot = 1.7998$) and the initial rotation velocity on the ZAMS was 50 km s^{-1}. The braking law of Kawaler (1988) was used to reproduce the magnetic braking experienced by low-mass stars during main-sequence evolution.

With the above assumptions, the characteristics of a stellar model depend on only four parameters: M, t, $Y_{\rm i}$ and $(Z/X)_{\rm i}$. The determination of the parameters that best reproduce the observational constraints was then performed in two

steps as described in Eggenberger & Carrier (2006). First, a grid of models with global properties in reasonable agreement (within 2σ) with the adopted spectroscopic constraints was constructed. Theoretical frequencies of $l \leq 2$ modes in the observed range of 590-1100 μHz were computed using the adiabatic pulsation code (Christensen-Dalsgaard 2008b) along with the characteristic frequency separations. The mean large separation was determined by considering only radial modes. The effects of incomplete modeling of the external layers on computed frequencies were taken into account using the empirical power law given by Kjeldsen et al. (2008). This correction was applied to theoretical frequencies using the solar calibrated value of the exponent ($b = 4.90$) and calculating the coefficient a for each stellar model.

Using spectroscopic measurements of [Fe/H], $T_{\rm eff}$ and $\log g$ together with the observed frequencies, a χ^2 minimization was performed to determine the set of model parameters that resulted in the best agreement with all observational constraints. The properties of the best model are listed in Table 3. This model correctly reproduces the spectroscopic measurements of the surface metallicity and $\log g$, but exhibits a slightly higher effective temperature. It is in good agreement with the asteroseismic data and in particular with the observed deviation of the $l = 1$ modes from asymptotic behavior. Model B is the best match from the family of solutions (also including Models C, E and G) with masses near 1.2 $M_{\odot}$.

4.3. *Model C*

The Garching Stellar Evolution Code (GARSTEC; Weiss & Schlattl 2008) is a one-dimensional hydrostatic code which does not include the effects of rotation. For the model calculations we used the OPAL equation of state (Rogers et al. 1996) complemented with the MHD equation of state at low temperatures (Hummer & Mihalas 1988), OPAL opacities for high temperatures (Iglesias & Rogers 1996) and Ferguson's opacities for low temperatures (Ferguson et al. 2005), the Grevesse & Sauval (1998) solar mixture, and the NACRE compilation of thermonuclear reaction rates (Angulo et al. 1999). Mixing is performed diffusively in convective regions using the mixing-length theory for convection in the formulation from Kippenhahn & Weigert (1990), and convective overshooting can optionally be implemented as a diffusive process with an exponential decay of the convective velocities in the radiative zone. The amount of mixing for overshooting depends on an efficiency parameter A calibrated with open clusters (typically $A = 0.016$). Atomic diffusion can be applied following the prescription of Thoul et al. (1994), and we use a plane-parallel Eddington grey atmosphere.

We started all of our calculations from the pre-main sequence phase. The value of the mixing-length parameter for convection was fixed ($\alpha = 1.791$ from our solar calibration), the Schwarzschild criterion for definition of convective boundaries was used, and we did not consider convective overshooting or atomic diffusion. We constructed a grid of models in the mass range between 1.0 $M_{\odot}$ and 1.3 $M_{\odot}$ (in steps of 0.01) for several [Fe/H] values from the spectroscopic analysis: 0.06, 0.09, 0.12, and 0.15. To convert the observed values into total metallicity, we applied a chemical enrichment law of $\Delta Y/\Delta Z = 2$ and used the primordial abundances from our solar calibration. We did not explore variations in either the hydrogen or helium abundances.

Once all of the tracks were computed, we restricted our analysis to those models contained within the spectroscopic uncertainties. For these cases, we calculated the oscillation frequencies using the adiabatic pulsation package (ADIPLS; Christensen-Dalsgaard 2008b) and looked for the model which best reproduced the large frequency separation (no surface correction was applied to the calculated frequencies). Several models were found to fulfill these requirements for each metallicity grid, and among those best fit models to the large frequency separation we then performed a χ^2 test to obtain the global best fit to the individual frequencies and the spectroscopic constraints. Our global best fit model came from the grid with [Fe/H] = 0.12, and the properties are listed in Table 3. This model reproduces well the observed mixed modes.

4.4. *Model D*

The Asteroseismic Modeling Portal (AMP) is a web-based tool tied to TeraGrid computing resources that uses the Aarhus stellar evolution code (ASTEC; Christensen-Dalsgaard 2008a) and adiabatic pulsation code (ADIPLS; Christensen-Dalsgaard 2008b) in conjunction with a parallel genetic algorithm (Metcalfe & Charbonneau 2003) to optimize the match to observational data (see Metcalfe et al. 2009). The models use the OPAL 2005 equation of state (see Rogers & Nayfonov 2002) and the most recent OPAL opacities (see Iglesias & Rogers 1996), supplemented by Kurucz opacities at low temperatures. The nuclear reaction rates come from Bahcall & Pinsonneault (1995), convection is described by the mixing-length theory of Böhm-Vitense (1958), and we can optionally include the effects of helium settling as described by Michaud & Proffitt (1993).

Each model evaluation involves the computation of a stellar evolution track from the zero-age main sequence (ZAMS) through a mass-dependent number of internal time steps, terminating prior to the beginning of the red giant stage. Rather than calculate the pulsation frequencies for each of the 200-300 models along the track, we exploit the fact that the average frequency separation of consecutive radial orders $\langle \Delta\nu_0 \rangle$ in most cases is a monotonically decreasing function of age (Christensen-Dalsgaard 1993). Once the evolution track is complete, we start with a pulsation analysis of the model at the middle time step and then use a binary decision tree—comparing the observed and calculated values of $\langle \Delta\nu_0 \rangle$—to select older or younger models along the track. This allows us to interpolate the age between the two nearest time steps by running the pulsation code on just 8 models from each stellar evolution track. The frequencies of each model are then corrected for surface effects following the prescription of Kjeldsen et al. (2008).

The genetic algorithm (GA) optimizes four adjustable model parameters, including the stellar mass (M) from 0.75 to 1.75 $M_{\odot}$, the metallicity (Z) from 0.002 to 0.05 (equally spaced in $\log Z$), the initial helium mass fraction ($Y_{\rm i}$) from 0.22 to 0.32, and the mixing-length parameter (α) from 1 to 3. The stellar age (t) is optimized internally during each model evaluation by matching the observed value of $\langle \Delta\nu_0 \rangle$ (see above). The GA uses two-digit decimal encoding, such that there are 100 possible values for each parameter within the specified ranges. Each run of the GA evolves a population of 128 models through 200 generations to find the optimal set of parameters, and we execute 4 independent runs with different random initialization to ensure that the best model identified is truly the global solution. The resulting properties of the optimal model are listed in Table 3.

The extreme values in this global fit arose from treating each spectroscopic constraint as equivalent to a single fre-

quency. Since the adopted spectroscopic errors are large, they provide much more flexibility for the models compared to the individual frequencies with relatively small errors. Consequently, the fitting algorithm found it advantageous to shift the effective temperature and metallicity by several σ from their target values to achieve significantly better agreement with the 22 oscillation frequencies. The improvement in the frequency match outweighed the degradation in the spectroscopic fit for the calculation of χ^2. The solution to this problem may be to calculate a separate value of χ^2 for the asteroseismic and spectroscopic constraints, and then average them to provide more equal weight to the two types of constraints. This is an important lesson for future automated searches, and explains why Model D does not align with either of the two major families of solutions.

4.5. *Model E*

We used the Yale Stellar Evolution Code (YREC; Demarque et al. 2008) in its non-rotating configuration to model KIC 11026764. All models were constructed with the OPAL equation of state (Rogers & Nayfonov 2002). We used OPAL high temperature opacities (Iglesias & Rogers 1996) supplemented with low temperature opacities from Ferguson et al. (2005). The NACRE nuclear reaction rates (Angulo et al. 1999) were used. We assumed that the current solar metallicity is that given by Grevesse & Sauval (1998). We have not explored the consequences of using the lower metallicity measurements of Asplund et al. (2005) or the intermediate metallicity measurements of Ludwig et al. (2009). We searched for the best fit within a fixed grid of models. There were eight separate grids defined by different combinations of the mixing-length parameter ($\alpha = 1.83$ or $\alpha = 2.14$), the initial helium abundance (either $Y_{\rm i} = 0.27$ or $Y_{\rm i}$ calculated assuming a $\Delta Y/\Delta Z = 2$, with $Y_{\rm i}$ for [Fe/H] = 0 being the current solar CZ helium abundance), and the amount of overshoot ($0\,H_p$ or $0.2\,H_p$). All models included gravitational settling of helium and heavy elements using the formulation of Thoul et al. (1994).

Our fitting method included two steps. In the first step, we calculated the average large frequency separation for the models and selected all of those that fit the observed separation within 3σ errors. We adopted the observed value of $\Delta\nu = 50.8 \pm 0.3\mu$Hz from Chaplin et al. (2010). A second cut was made using the effective temperature: all models within $\pm 2\sigma$ of the observed value were chosen. A third cut was made using the frequencies of the three lowest-frequency $l = 0$ modes. Given the small variation in mass, this process was effectively a radius cut. The selected models had radii around $2R_\odot$. Note that the Yale-Birmingham radius pipeline (Basu et al. 2010) finds a radius of $2.18^{+0.04}_{-0.05}R_\odot$ for this star using the adopted values of $\Delta\nu$, $T_{\rm eff}$, $\log g$ and [Fe/H]. In the second step of the process, we made a finer grid in mass and age around the selected values and then compared the models with the observed set of frequencies. The properties of our best fit model are listed in Table 3. This model was constructed with $Y_{\rm i} = 0.27$, $Z_{\rm i} = 0.0147$ and core overshoot of $0.2\,H_p$. We were unable to find a good model without core overshoot.

4.6. *Model F*

We modeled KIC 11026764 with the Catania Astrophysical Observatory version of the GARSTEC code (Bonanno et al. 2002) using a grid-based approach. The input physics of this stellar evolution code included the OPAL 2005 equation of state (Rogers & Nayfonov 2002) and the OPAL opacities (Iglesias & Rogers 1996) complemented in the low temperature regime with the tables of Alexander & Ferguson (1994). The nuclear reaction rates were taken from the NACRE collaboration (Angulo et al. 1999) and the standard mixing-length formalism for convection was used (Kippenhahn & Weigert 1990). Microscopic diffusion of hydrogen, helium and all of the major metals can optionally be taken into account. The outer boundary conditions were determined by assuming an Eddington grey atmosphere.

A grid of evolutionary models was computed to span the 1σ uncertainties in the spectroscopic constraints obtained from ground based observations. When a given evolutionary track was in the error box, a maximum time step of 20 Myr was chosen and the frequencies were computed with the ADIPLS code. A non-uniform grid of mass in the range 1.0-1.24 $M_\odot$, helium abundance in the range $Y_{\rm i} = 0.26$-0.31, mixing-length parameter $\alpha = 1.6$-1.9 and initial surface heavy-element abundances $(Z/X)_{\rm i} = 0.022$-0.029 was scanned. A global optimization strategy was implemented by minimizing the χ^2 for all of the $l = 0$, $l = 1$ and $l = 2$ modes. The empirical surface effect, as discussed by Kjeldsen et al. (2008), was used to correct all theoretical frequencies. The properties of the best model with heavy-element diffusion and surface corrected frequencies are listed in Table 3.

4.7. *Model G*

We used a version of the Aarhus stellar evolution code (ASTEC; Christensen-Dalsgaard 2008a) which includes the OPAL 2001 equation of state (Rogers et al. 1996), OPAL opacities (Iglesias & Rogers 1996), Bahcall & Pinsonneault (1995) nuclear cross sections and the mixing-length formalism (Böhm-Vitense 1958) for convection. We computed several grids of models by varying all of the input parameters within the range of the observed errors (Chaplin et al. 2010). In particular we calculated evolutionary tracks by varying the input mass in the range $M = 0.9$-1.2 $M_\odot$, the metallicity in the range $Z = 0.009$-0.03, and the hydrogen abundance in the range $X = 0.67$-0.7. We also adopted different values of the mixing-length parameter in the range $\alpha = 1.67$-1.88. We calculated additional evolutionary models using the Canuto & Mazzitelli (1992) convection formulation. The mixing-length parameter α of the CM formulation was chosen in the range $\alpha = \alpha_{\rm CM} = 0.9$-$1.0$. To obtain the deviation from asymptotic behavior observed in the $l = 1$ modes (the mixed modes) we did not include overshooting in the calculation, following the conclusion of Di Mauro et al. (2003). These models are distinct from the grid used to produce Model A, not only because they employ a slightly older EOS and nuclear reaction rates, but also because the grid search included α and calculated fewer models within the specified range of parameter values. We used the adiabatic oscillation code (ADIPLS; Christensen-Dalsgaard 2008b) to calculate the p-mode eigenfrequencies with harmonic degree $l = 0$-2. The characteristics of the model which best fits the observations are listed in Table 3.

4.8. *Model H*

For the evolution calculations we used the publicly available Dartmouth stellar evolution code (DSEP; Chaboyer et al. 2001; Guenther et al. 1992; Dotter et al. 2007), which is based on the code developed by Pierre Demarque and his students (Larson & Demarque 1964; Demarque & Mengel 1971). The

input physics includes high temperature opacities from OPAL (Iglesias & Rogers 1996), low temperature opacities from Ferguson et al. (2005), the nuclear reaction rates of Bahcall & Pinsonneault (1992), helium and heavy-element settling and diffusion (Michaud & Proffitt 1993), and Debye-Hückel corrections to the equation of state (Guenther et al. 1992). The models employ the standard mixing-length theory. Convective core overshoot is calculated assuming that the extent is proportional to the pressure scale height at the boundary (Demarque et al. 2004). The models used the standard conversion from [Fe/H] and $\Delta Y/\Delta Z$ to Z and Y (Chaboyer et al. 1999). The oscillation frequencies were computed using the adiabatic oscillation codes of Kosovichev (1999) and Christensen-Dalsgaard (2008b). No surface corrections were applied.

The strategy to find a model matching the observed spectroscopic constraints involved calculating a series of evolutionary tracks in the $\log g$-$T_{\rm eff}$ plane for a mass range of 1.0-1.3 $M_\odot$, heavy-element abundance Z = 0.01-0.03, initial helium abundance $Y_{\rm i}$ = 0.25-0.30, and mixing-length parameter α = 1.70-1.75. We then selected the models closest to the target values within half of the specified uncertainties. All models for the search were calculated assuming an overshoot parameter $\alpha_{\rm ov}$ = 0.2, and included element diffusion. For comparison, the corresponding models without diffusion and convective overshoot were also calculated. The oscillation spectra were matched to the observed frequencies, first by comparing the frequencies of radial (l = 0) modes with the corresponding observed frequencies, and then selecting a model with the closest frequency values for the l = 1 and l = 2 modes. The properties of the final model are listed in Table 3. This model matches the observed frequencies quite well except for the first two l = 1 modes, which deviate by about 12-13 μHz. Our search demonstrated that the behavior of the mixed mode frequencies is sensitive to element diffusion and convective overshoot. This requires further investigation.

4.9. *Model I*

To characterize KIC 11026764 we constructed a grid of stellar models with the CESAM code (Morel 1997), and computed their oscillation frequencies with the adiabatic oscillation code FILOU (Suárez 2002; Suárez & Goupil 2008). Opacity tables were taken from the OPAL package (Iglesias & Rogers 1996), complemented at low temperatures ($T \leq 10^4\,K$) with the tables provided by Alexander & Ferguson (1994). The atmosphere was constructed from a Eddington T-τ relation and was assumed to be grey. The stellar metallicity (Z/X) was derived from the [Fe/H] value assuming $(Z/X)_\odot = 0.0245$ (Grevesse & Noels 1993), $Y_{\rm pr}$ = 0.235 and $Z_{\rm pr}$ = 0 for the primordial helium and heavy-element abundances, and a value $\Delta Y/\Delta Z$ = 2 for the enrichment ratio. No microscopic diffusion of elements was considered.

The main strategy was to search for representative equilibrium models of the star in a database of 5×10^5 equilibrium models, querying for those matching the global properties of the star, including the effective temperature, gravity and metallicity. Using this set of models, we then applied the asteroseismic constraints, including the individual frequencies and large separations. The global fitting method involved a χ^2 minimization, taking into account all of the observational constraints simultaneously. No correction for surface effects was applied, and no *a priori* information on mode identification was assumed when fitting the individual frequencies. The properties of the best model we found is listed in Table 3, and includes overshooting with $\alpha_{\rm ov}$ = 0.3. Note that the analysis did not adopt the identifications of spherical degree (l) from §2, and it included l = 3 modes to perform the match. As a consequence, the final result is much different than any of the others and it does not fall into either of the two major families of solutions.

4.10. *Model J*

The SEEK procedure makes use of a large grid of stellar models computed with the Aarhus stellar evolution code (ASTEC; Christensen-Dalsgaard 2008a). It compares the observations with every model in the grid and makes a probabilistic assessment, with the help of Bayesian statistics, about the global properties of the star. The model grid includes 7,300 evolution tracks containing 5,842,619 individual models. Each track begins at the ZAMS and continues to the red giant branch or a maximum age of t = 15 Gyr. The tracks are separated into 100 subsets with different combinations of metallicity Z, initial hydrogen content $X_{\rm i}$ and mixing-length parameter α. These combinations are separated into two regularly spaced and interlaced subgrids. The first subgrid comprises tracks with $Z = [0.005, 0.01, 0.015, 0.02, 0.025, 0.03]$, $X_{\rm i} = [0.68, 0.70, 0.72, 0.74]$, and $\alpha = [0.8, 1.8, 2.8]$ while the second subset has $Z = [0.0075, 0.0125, 0.0175, 0.0225, 0.0275]$, $X_{\rm i} = [0.69, 0.71, 0.73]$, $\alpha = [1.3, 2.3]$. Every subset is composed of 73 tracks with masses between 0.6 and 3.0 $M_\odot$. The spacing in mass between the tracks is 0.02 $M_\odot$ from 0.6 to 1.8 $M_\odot$ and 0.1 from 1.8 to 3.0 $M_\odot$. A relatively high value of $Y_\odot = 0.2713$ and $Z_\odot = 0.0196$ for the Sun has been used for the standard definition of [Fe/H] in SEEK. This value is used to calibrate solar models from ASTEC to the correct luminosity (Christensen-Dalsgaard 1998). The input physics include the OPAL equation of state, opacity tables from OPAL (Iglesias & Rogers 1996) and Alexander & Ferguson (1994), and the metallic mixture of Grevesse & Sauval (1998). Convection is treated according to the mixing-length theory of Böhm-Vitense (1958) with the convective efficiency characterized by the mixing-length to pressure height scale ratio α, which varies across the grid of models. Diffusion and overshooting were not included.

The grid allows us to map the physical input parameters of the model $\mathbf{p} \equiv \{M, t, Z, X_{\rm i}, \alpha\}$ into the grid of observable quantities $\mathbf{q^g} \equiv \{\Delta\nu, \delta\nu, T_{\rm eff}, \log g, [{\rm Fe/H}], ...\}$, defining the transformation

$$\mathbf{q^g} = \mathcal{K}(\mathbf{p}). \tag{4}$$

We compare these quantities to the observed values $\mathbf{q^{obs}}$ with the help of a likelihood function $\mathcal{L}$,

$$\mathcal{L} = \left(\prod_{i=0}^{n} \frac{1}{\sqrt{2\pi}\sigma_i} \right) \exp(-\chi^2/2), \tag{5}$$

and the usual χ^2 definition

$$\chi^2 = \frac{1}{N} \sum_{i=0}^{N} \left(\frac{q_i^{\rm obs} - q_i^{\rm g}}{\sigma_i} \right)^2 \tag{6}$$

where σ_i is the estimated error for each observation $q_i^{\rm obs}$, and N is the number of observables. The maximum likelihood is then combined with the prior probability of the grid f_0 to yield the posterior, or the resulting probability density

$$f(\mathbf{p}) \propto f_0(\mathbf{p}) \mathcal{L}(\mathcal{K}(\mathbf{p})). \tag{7}$$

Table 4
Final model-fitting results for KIC 11026764.

Model	$M/M_\odot$	Z_s	Y_s	α	t (Gyr)	$L/L_\odot$	$R/R_\odot$	$T_{\rm eff}$(K)	$\log g$	[Fe/H]	χ^2
FA...	1.13	0.017	0.305	1.64	5.268	4.141	2.036	5778	3.872	+0.009	3.69
AA..	1.13	0.019	0.291	1.70	5.977	3.520	2.029	5556	3.877	+0.051	6.11
AA′..	1.13	0.019	0.291	1.70	5.935	3.454	2.026	5534	3.877	+0.031	7.40
GA..	1.10	0.017	0.296	1.88	6.100	3.420	2.010	5539	3.870	+0.004	78.05
CA...	1.13	0.019	0.291	1.70	6.204	3.493	2.030	5546	3.876	+0.050	152.91
EA...	1.12	0.019	0.291	1.70	6.683	3.202	2.029	5424	3.870	+0.050	230.58
AB...	1.23	0.018	0.242	1.80	5.869	3.804	2.083	5591	3.890	−0.010	6.97
AB′..	1.20	0.024	0.276	1.80	5.994	3.460	2.072	5475	3.884	+0.146	7.26
BB...	1.22	0.021	0.270	1.80	5.153	4.190	2.061	5758	3.896	+0.072	7.57
FB...	1.24	0.021	0.280	1.79	4.993	4.438	2.092	5800	3.890	+0.091	8.52
EB...	1.22	0.013	0.232	1.80	4.785	4.651	2.079	5882	3.890	−0.130	18.54
CB...	1.24	0.015	0.250	1.80	5.064	4.696	2.089	5887	3.892	−0.080	45.84
J′....	1.27	0.021	0.270	1.52	4.260	4.011	2.105	5634	3.892	+0.080	···
±error	0.09	0.003	0.024	0.74	1.220	0.371	0.064	81	0.020	±0.060	···
K′...	1.20	0.022	0.278	1.80	5.980	3.700	2.026	5619	3.900	+0.070	···
±error	0.04	0.003	0.003	···	0.610	0.300	0.027	79	0.006	±0.060	···

This probability density can be integrated to obtain the value and uncertainty for each of the parameters, as listed in Tables 3 and 4. It can also be projected onto any plane to get the correlation between two parameters, as shown in Appendix B. The details of the SEEK procedure, including the choice of priors, and an introduction to Bayesian statistics can be found in Quirion, Christensen-Dalsgaard & Arentoft (2010).

SEEK uses the large and small separations and the median frequency of the observed modes as asteroseismic inputs. Values of $\Delta\nu_0 = 50.68 \pm 1.30$ (computed with $l = 0$ modes only) and $\delta\nu_{0,2} = 4.28 \pm 0.73$ (computed from $l = 0, 2$ modes) were derived from *Kepler* data around a central value 900 μHz. Each separation is the mean of the individual observed separations, while the error is the standard deviation of the individual values from the mean. These values differ slightly from those given in Chaplin et al. (2010) because they are calculated from the individual frequencies rather than derived from the power spectrum. Using these asteroseismic inputs along with the initial spectroscopic constraints, we obtained the parameters listed in Table 3. For a SEEK analysis of the importance of the asteroseismic constraints, see Appendix B.

4.11. *Model K*

To investigate how well we can find an appropriate model without comparing individual oscillation frequencies, we used the RADIUS pipeline (Stello et al. 2009a), which takes $T_{\rm eff}$, $\log g$, [Fe/H], and $\Delta\nu$ as the only inputs to find the best fitting model. The value of $\Delta\nu = 50.8 \pm 0.3\,\mu$Hz from Chaplin et al. (2010) was adopted. The pipeline is based on a large grid of ASTEC models (Christensen-Dalsgaard 2008a) using the EFF equation of state (Eggleton et al. 1973). We use the opacity tables of Rogers & Iglesias (1995) and Kurucz (1991) for $T < 10^4$ K with the solar mixture of Grevesse & Noels (1993). Rotation, overshooting and diffusion were not included. The grid was created with fixed values of the mixing-length parameter ($\alpha = 1.8$) and the initial hydrogen abundance ($X_i = 0.7$). The resolution in $\log Z$ was 0.1 dex between $0.001 < Z < 0.055$, and the resolution in mass was 0.01 $M_\odot$ from 0.5 to 4.0 $M_\odot$. The evolution begins at the ZAMS and continues to the tip of the red giant branch. To convert between the model values of Z and the observed [Fe/H], we used $Z_\odot = 0.0188$ (Cox 2000).

We made slight modifications to the RADIUS approach described by Stello et al. (2009a). First, the large frequency separation was derived by scaling the solar value (Kjeldsen & Bedding 1995) instead of calculating it directly from the model frequencies. Although there is a known systematic difference between these two ways of deriving $\Delta\nu$, the effect is probably below the 1% level (Stello et al. 2009b; Basu et al. 2010). Second, we pinpointed a single best-fitting model based on a χ^2 formalism that was applied to all models within $\pm 3\sigma$ of the observed properties. The properties of the best fitting model are listed in Table 3. This model shows a frequency pattern in the échelle diagram that looks very similar to the observations if we allow a small tweaking of the adopted frequency separation (52.1μHz) used to generate the échelle. This basically means that we found a model that homologously represents the observations quite well. In particular, we see relative positions of the $l = 1$ mode frequencies that are very similar to those observed.

5. MODEL-FITTING RESULTS

Based on the value of χ^2 from the initial search in §4, we adopted two reference models (Models A and B in Table 3) each constructed with a very different set of input physics, but almost equally capable of providing a good match to the observations. Note that Model A does not include overshoot or diffusion, while Model B includes overshoot, diffusion and a full treatment of rotation. These two models differ significantly in the optimal values of the mass, effective temperature, metallicity and luminosity, but they both agree with the observational constraints at approximately the same level ($\chi^2 \sim 10$). With the exceptions of Models D and I (see subsections above), the other independent analyses generally fall into the two broad families of solutions defined by Models A and B. The lower mass family includes Models A, F, H, J and K, while the higher mass family includes Models B, C, E and

G. We identified several additional asteroseismic constraints from the maximal frequency set (see §2) and we adopted revised spectroscopic constraints from VWA (see §3) to refine our analysis of Models A and B using several different codes.

5.1. *Refining the Best Models*

Comparing the theoretical frequencies of Models A and B with the maximal frequency set from §2, we identified four of the seven additional oscillation modes that could be used for refined model-fitting (see Table 1). Recall that the maximal frequency set comes from the *individual analysis* with the smallest *rms* deviation with respect to the maximal list, so the frequencies of the modes from the minimal set are slightly different in the maximal set. Without any additional fitting, these subtle frequency differences improve the χ^2 of Models A and B when comparing them to those modes from the maximal set that are also present in the minimal set. There is one additional $l = 0$ mode ($n = 12$) and three additional $l = 2$ modes ($n = 11, 16, 19$) in the maximal set that are within 3σ of frequencies in both Models A and B. Considering the very different input physics of these two models, we took this agreement as evidence of the reliability of these four additional frequencies and we incorporated them as constraints for our refined model-fitting. Two of the remaining frequencies in the maximal set ($n = 12, l = 1$ and 2) were not present in either Models A or B, while one ($n = 10, l = 2$) had a close match in Model B but not in Model A. We excluded these three modes from the refined model-fitting. Given that the $l = 1$ modes provide the strongest constraints on the models (see §5.2), the additional $l = 0$ and $l = 2$ modes are expected to perturb the final fit only slightly.

In addition to the 26 oscillation frequencies from the maximal set, we also included stronger spectroscopic constraints in the refined model-fitting by adopting the results of the VWA analysis instead of using the mean atmospheric parameters from the preliminary analyses (see §3.3). Although the uncertainties on all three parameters are considerably smaller from the VWA analysis, the actual values only differ slightly from the initial spectroscopic constraints. These were just three of the 25 constraints used to calculate the χ^2 and rank the initial search results in Table 3. Since the 22 frequencies from the minimal set were orders of magnitude more precise, they dominated the χ^2 determination. Although the spectroscopic constraints from VWA are more precise than the initial atmospheric parameters, they are still much less precise than the frequencies and should only perturb the χ^2 ranking slightly. Consequently, we do not need to perform a new global search after adopting the additional and updated observational constraints.

Several modeling teams used the updated asteroseismic and spectroscopic constraints for refined model-fitting with a variety of codes. Each team started with the parameters of Models A and B from Table 3, and then performed a local optimization to produce the best match to the observations within each family of solutions. The results of this analysis are shown in Table 4, where the refined Models A and B are ranked separately by their final χ^2 value. Each model is labeled with a letter from Table 3 to identify the modeling team, followed by either A or B to identify the family of solutions. The two pipeline approaches labeled J′ and K′ simply adopted the revised constraints to evaluate any shift in the optimal parameter estimates and errors. Note that both the SEEK and RADIUS pipelines identified parameters in the high-mass family

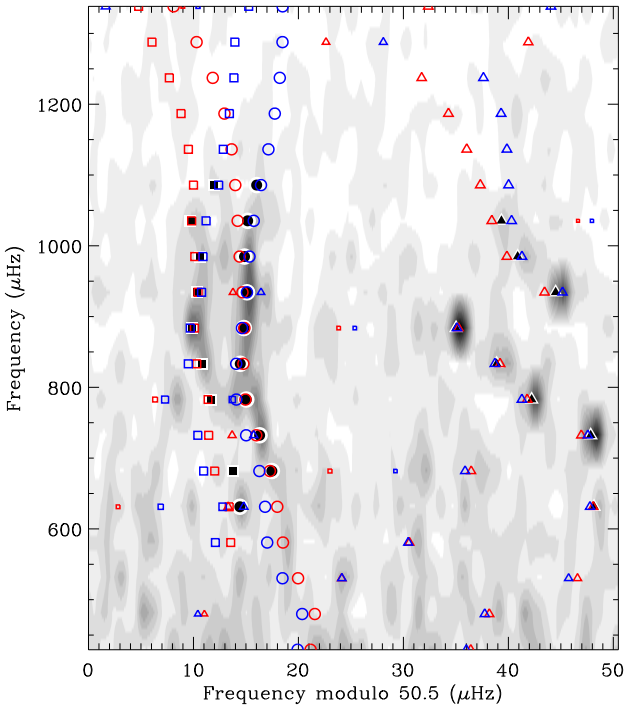

Figure 3. An échelle diagram showing the 26 frequencies from the maximal set that were used as constraints (solid points) with the frequencies of Models AA (blue) and AB (red) for comparison. The star exhibits modes with $l = 0$ (circles), $l = 1$ (triangles), and $l = 2$ (squares). A greyscale map showing the power spectrum (smoothed to 1 μHz resolution) is included in the background for reference.

of solutions when using the revised constraints, but the low-mass family was only marginally suboptimal. The apparent bifurcation of results in Table 4 into two values of α arises from the decision of most modelers to fix this parameter in each case to the original value from Table 3. For each family of solutions, the modeling teams adopted the appropriate input physics: neglecting overshoot and diffusion for the refined Models A, while including both ingredients for the refined Models B. One team produced two additional models (labeled AA′ and AB′) to isolate the effect of input physics on the final results. Model AA′ started from the parameters of Model A but included overshoot and helium settling, while Model AB′ searched in the region of Model B but neglected overshoot and diffusion.

5.2. *Stellar Properties & Error Analysis*

An inspection of the results in Table 4 reveals that models in either family of solutions can provide a comparable match to the observational constraints. This ambiguity cannot be attributed to the input physics, since the models that sample all four combinations of the input physics and family of solutions (AA, AA′, AB, AB′) have comparable χ^2 values. The individual frequencies of these models all provide a good fit to the data, including the $l = 1$ mixed modes. The observations are compared to two representative models in Figure 3 using an échelle diagram, where we divide the frequency spectrum into segments of length $\langle\Delta\nu\rangle$ and plot them against the oscillation frequency. This representation of the data aligns modes with the same spherical degree into roughly vertical columns, with $l = 0$ modes shown as circles, $l = 1$ modes shown as triangles, and $l = 2$ modes shown as squares. The 26 modes from the maximal frequency set that were included

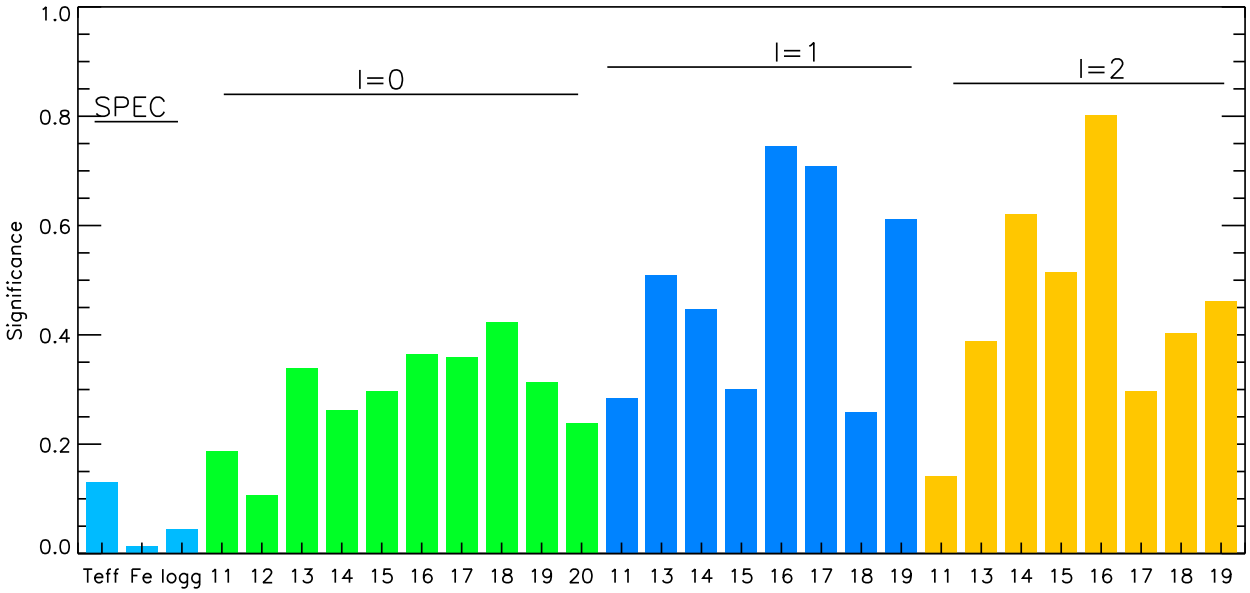

Figure 4. The significance S_i of each observational constraint in determining the parameters of Model AA. Each oscillation frequency is labeled with the reference radial order from Table 1, and the degrees l = 0, 1 and 2 are shown sequentially in different shades from left to right.

in the final fit are indicated with solid points. Open points indicate the model frequencies, with Model AA shown in blue and Model AB shown in red. A greyscale map of the power spectrum (smoothed to 1 μHz resolution) is included in the background for reference. The different models appear to be sampling comparable local minima in a correlated parameter space. Without additional constraints, we have no way of selecting one of these models over the other.

We can understand the two families of models by considering the general properties of subgiant stars, where a wide range of masses can have the same stellar luminosity with minor adjustments to the input physics and other model parameters—in particular the helium mass fraction. This degeneracy between mass and helium abundance has been discussed in the modeling of specific subgiant stars (e.g. Fernandes & Monteiro 2003; Pinheiro & Fernandes 2010; Yang & Meng 2010), and it adds a large uncertainty to the already difficult problem of determining the helium abundance in main-sequence stars (e.g. Vauclair et al. 2008; Soriano & Vauclair 2010). The luminosity of stellar models on the subgiant branch is mainly determined by the amount of energy produced at the edge of the helium core established during the main-sequence phase. The rate of energy production depends on the temperature and the hydrogen abundance in that layer. As a consequence it is possible to find models at the same luminosity with quite different values of total mass, by adjusting the other parameters to yield the required temperature at the edge of the helium core. Fortunately, for subgiant stars the presence of mixed modes can provide additional constraints on the size of the helium core. For KIC 11026764 this mixed mode constraint significantly reduces the range of possible masses to two specific intervals, where the combination of stellar mass and core size are compatible with the atmospheric parameters and the frequencies of the mixed modes.

Regardless of which family of solutions is a better representation of KIC 11026764, the parameter values in Table 4 already yield precise determinations of some of the most interesting stellar properties—in particular, the asteroseismic age and radius. If we consider only the four models that were produced by the same modeling team with an identical fitting method (the ASTEC models: AA, AA′, AB, AB′), we can calculate the mean value and an internal (statistical) uncertainty in isolation from external (systematic) errors arising from differences between the various codes and methods. The asteroseismic ages of the two families of solutions range from 5.87 to 5.99 Gyr, with a mean value of $t = 5.94 \pm 0.05$ Gyr. The stellar radii of the two families range from 2.03 to 2.08 $R_\odot$, with a mean value of $R = 2.05 \pm 0.03$ $R_\odot$. The luminosity ranges from 3.45 to 3.80 $L_\odot$, with a mean value of $L = 3.56 \pm 0.14$ $L_\odot$. These are unprecedented levels of precision for an isolated star, despite the fact that the stellar mass is still ambiguous at the 10% level. Of course, *precision* does not necessarily translate into *accuracy*, but we can evaluate the possible systematic errors on these determinations by looking at the distribution of parameter values for the entire sample of modeling results, not just those from ASTEC.

Considering the full range of the best models ($\chi^2 < 10$) in Table 4, there is broad agreement on the value of the stellar radius. The low value of 2.03 $R_\odot$ is from one of the ASTEC models considered above, while the high value of 2.09 $R_\odot$ is from the Catania-GARSTEC code, leading to a systematic offset of $^{+0.04}_{-0.02}$ $R_\odot$ compared to the mean ASTEC value. There is a slightly higher dispersion in the values of the asteroseismic age. Again considering only the best models, we find a full range for the age as low as 4.99 Gyr from Catania-GARSTEC up to 5.99 Gyr from ASTEC, for a systematic offset of $^{+0.05}_{-0.95}$ Gyr relative to the ASTEC models. The best models exhibit the highest dispersion in the values of the luminosity, with a low estimate of 3.45 $L_\odot$ from ASTEC and a high value of 4.44 $L_\odot$ from Catania-GARSTEC. These models establish a systematic offset of $^{+0.88}_{-0.11}$ $L_\odot$ compared to the ASTEC results.

To evaluate the relative contribution of each observational constraint to the final parameter determinations, we can study the significance S_i using singular value decomposition (SVD; see Brown et al. 1994). An observable with a low value of S_i has little influence on the solution, while a high value of S_i indicates an observable with greater impact. The

significance of each observable in determining the parameters of KIC 11026764 for Model AA is shown in Figure 4. From left to right we show the spectroscopic constraints followed by the $l = 0$, 1 and 2 frequencies labeled with the reference radial order from Table 1, and each group of constraints is shown in a different shade. It is immediately clear that the $l = 1$ and $l = 2$ frequencies have more weight in determining the parameters. If we examine how the significance of each spectroscopic constraint changes when we combine them with modes of a given spherical degree, we can quantify the impact of each set of frequencies because the information content of the spectroscopic data does not change. The spectroscopic constraints contribute more than 25% of the total significance when combined with the $l = 0$ modes (13% from the effective temperature alone), indicating that these two sets of constraints contain redundant information. By contrast, the total significance of the spectroscopic constraints drops to 4% for the $l = 2$ modes, and 7% when combined with the $l = 1$ modes—confirming that these frequencies contain more independent information than the $l = 0$ modes, as expected from the short evolutionary timescale for mixed modes. Although the significance of the atmospheric parameters on the final solution appears to be small, we emphasize that accurate spectroscopic constraints are essential for narrowing down the initial parameter space.

6. SUMMARY & DISCUSSION

We have determined a precise asteroseismic age and radius for KIC 11026764. Although no planets have yet been detected around this star, similar techniques can be applied to exoplanet host stars to convert the relative planetary radius determined from transit photometry into an accurate absolute radius—and the precise age measurements for field stars can provide important constraints on the evolution of exoplanetary systems. By matching stellar models to the individual oscillation frequencies, and in particular the $l = 1$ mixed mode pattern, we determined an asteroseismic age and radius of $t = 5.94 \pm 0.05(\mathrm{stat})^{+0.05}_{-0.95}(\mathrm{sys})$ Gyr and $R = 2.05 \pm 0.03(\mathrm{stat})^{+0.04}_{-0.02}(\mathrm{sys})\ R_\odot$. This represents an order of magnitude improvement in the age precision over pipeline results—which fit only the mean frequency separations—while achieving comparable or slightly better precision on the radius (cf. Models J′ and K′ in Table 4). The systematic uncertainties on the radius are almost negligible, while the model-dependence of the asteroseismic age yields impressive accuracy compared to other age indicators for field stars (see Soderblom 2010). Whatever the limitations on absolute asteroseismic ages, studies utilizing a single stellar evolution code can precisely determine the *chronology* of stellar and planetary systems.

The $l = 1$ mixed modes in KIC 11026764, shifted from regularity by avoided crossings, play a central role in constraining the models. Bedding et al. (in prep.) have pointed out the utility of considering the frequencies of the avoided crossings themselves, since they reflect the g-mode component of the eigenfunction that is trapped in the core (Aizenman et al. 1977). The avoided crossing frequencies are revealed by the distortions in the $l = 1$ modes, which are visible as rising branches in Figure 1. For Model AA, marked by the vertical line, we see that the frequencies of the first four avoided crossings are $G_1 \approx 1270\,\mu$Hz, $G_2 \approx 920\,\mu$Hz, $G_3 \approx 710\,\mu$Hz and $G_4 \approx 600\,\mu$Hz. Each of these avoided crossings produces a characteristic feature in the échelle diagram that can be matched to the observations. Indeed, the observed power spectrum of KIC 11026764 (greyscale in Figure 3) shows a clear feature that matches G_2 and another, slightly less clear, that matches G_3. The avoided crossing at G_1 that is predicted by the models lies outside the region of detected modes, but it is possible that additional data expected from the *Kepler Mission* will confirm its existence. We also note a peak in the observed power spectrum at 586 μHz (greyscale in Figure 3) that lies close to an $l = 1$ mixed mode in the models, and also at 766 μHz near an $l = 2$ mixed mode. Again, additional data are needed for confirmation.

It is interesting to ask whether all of the models discussed in this paper have the same avoided crossing identification. For example, are there any models that fit the observed frequencies but for which the avoided crossing at $920\,\mu$Hz corresponds to G_1 instead of G_2? This would imply a different local minimum in parameter space, and a different location in the p-g diagram introduced by Bedding et al. Although this may be the case for some of the models in Table 3 from the initial search, all of the models listed in Table 4 have the avoided crossing identification described above.

The observed structure of the $l = 1$ ridge suggests relatively strong coupling between the oscillation modes. At frequencies above the observed range, the best models suggest that the unperturbed $l = 1$ ridge would align vertically near 40 μHz in the échelle diagram (see Figure 3). It is evident from Figure 1 that at a given age the frequencies of numerous p-modes are affected by the rising g-mode frequency, and this manifests itself in the échelle diagram with several modes deviating from the location of the unperturbed ridge on either side of the avoided crossing (Deheuvels & Michel 2009). Stronger coupling suggests a smaller evanescent zone between the g-mode cavity in the core and the p-mode cavity in the envelope. Although the evanescent zone will be larger for $l = 2$ modes, the strength of the coupling for the $l = 1$ modes raises the possibility that weakly mixed $l = 2$ modes—like those near 766 μHz in Model AA—may be observable in longer time series data from continued observations by *Kepler*.

It is encouraging that with so many oscillation frequencies observed, the impact of an incorrect mode identification appears to be minimal. For example, the models suggest that the lowest frequency $l = 0$ mode in Table 1 may actually be on the $l = 2$ ridge—or it could even be an $l = 1$ mixed mode produced by the G_4 avoided crossing. However, the influence of the other observational constraints is sufficient to prevent any serious bias in the resulting models. Even so, adopting either of these alternate identifications for the lowest frequency $l = 0$ mode would cut the χ^2 of Model AB nearly in half.

Despite a 10% ambiguity in the stellar mass, we have determined a luminosity for KIC 11026764 of $L = 3.56 \pm 0.14(\mathrm{stat})^{+0.88}_{-0.11}(\mathrm{sys})\ L_\odot$. With the radius so well determined from asteroseismology, differences of 200-300 K in the effective temperatures of the models are largely responsible for the uncertainties in the luminosity. These differences are generally correlated with the composition—hotter models at a given mass tend to have a higher helium mass fraction and lower metallicity, while cooler models tend to be relatively metal-rich. The adopted spectroscopic constraints fall in the middle of the range of temperatures and metallicities for the two families of models, and leave little room for substantial improvement. Perhaps the best chance for resolving the mass ambiguity, aside from additional asteroseismic constraints, is a direct measurement of the luminosity. Although *Kepler* was not optimized for astrometry, it will eventually provide high-

quality parallaxes (Monet et al. 2010). The resulting luminosity error is expected to be dominated by uncertainties in the bolometric correction ($\sim$0.02 mag) and the amount of interstellar reddening ($\sim$0.01 mag), although saturation from this bright target may present additional difficulties. This should lead to a luminosity precision near 3%, which would be sufficient to distinguish between our two families of solutions for KIC 11026764.

Funding for the *Kepler Mission* is provided by NASA's Science Mission Directorate. This work was supported in part by NASA grant NNX09AE59G. Computer time was provided by TeraGrid allocation TG-AST090107. The National Center for Atmospheric Research is sponsored by the U.S. National Science Foundation. Observations were made with the Nordic Optical Telescope, operated on the island of La Palma jointly by Denmark, Finland, Iceland, Norway, and Sweden, in the Spanish Observatorio del Roque de los Muchachos of the Instituto de Astrofisica de Canarias. TA gratefully acknowledges support from the Programme National de Physique Stellaire of INSU/CNRS. GD, P-OQ, CK, JC-D and HK are grateful for financial support from the Danish Natural Science Research Council. J.M-Ż acknowledges MNiSW grant N203 014 31/2650. MJPFGM acknowledges financial support from project TDC/CTE-AST/098754/2008 from FCT & FEDER, Portugal. TRB and DS acknowledge financial support from the Australian Research Council. WJC, YE, A-MB, STF, SH and RN acknowledge the support of the UK Science and Facilities Technology Council. OLC and P-OQ acknowledge support from HELAS, a major international collaboration funded by the European Commission's Sixth framework program. SGS acknowledges support from the FCT (Portugal) through grants SFRH/BPD/47611/2008 and PTDC/CTE-AST/66181/2006. The authors wish to thank the Kepler Science Team and everyone who helped make the *Kepler Mission* possible.

REFERENCES

Aerts, C., Christensen-Dalsgaard, J., & Kurtz, D. W. 2010, Asteroseismology, Springer, (ISBN: 978-1-4020-5178-4)
Aizenman, M., Smeyers, P., & Weigert, A. 1977, A&A, 58, 41
Alexander, D. R. & Ferguson, J. W. 1994, ApJ, 437, 879
Anderson, E. R., Duvall, T. L. Jr., Jefferies, S. M., 1990, ApJ, 364, 699
Angulo, C., Arnould, M., Rayet, M., et al. 1999, Nucl. Phys. A., 656, 3
Appourchaux, T., Michel, E., Auvergne, M., et al., 2008, A&A, 488, 705
Asplund, M., Grevesse, N., & Sauval, A. J. 2005, ASP Conf., 336, 25
Bahcall, J. N., & Pinsonneault, M. H. 1992, Rev Mod. Phys., 64, 885
Bahcall J. N., Pinsonneault M. H., 1995, Rev. Mod. Phys., 67, 781
Basu, S., Chaplin, W. J., Elsworth, Y. 2010, ApJ, 710, 1596
Bedding, T. R., et al. 2007, ApJ, 663, 1315
Bedding, T. R., et al. 2010, ApJ, 713, 935
Benomar, O., Appourchaux, T., Baudin, F., 2009, A&A, 506, 15
Biazzo, K., Randich, S., Palla, F. 2010, A&A, in preparation
Böhm-Vitense, E. 1958, Zeitschrift fur Astrophysik, 46, 108
Bonanno, A., Schlattl, H., Paternó L., 2002, A&A, 390, 1115
Borucki, W. J., et al. 2007, ASP. Conf, 366, 309
Brown, T. M., et al. 1994, ApJ, 427, 1013
Bruntt H., et al. 2004, A&A, 425, 683
Bruntt H., De Cat P., Aerts, C. 2008, A&A, 478, 487
Bruntt H., et al. 2010a, MNRAS, accepted (arXiv:1002.4268)
Bruntt, H., et al. 2010b, A&A, accepted (arXiv:1005.3208)
Campante, T. L., et al. 2010, MNRAS, submitted
Canuto, V. M. & Mazzitelli, I. 1992, ApJ, 389, 724
Carrier, F., Eggenberger, P., & Bouchy, F. 2005, A&A, 434, 1085
Castelli, F., & Kurucz, R. L. 2003, IAU Symp., 210, 20
Chaboyer, B., & Zahn, J.-P. 1992, A&A, 253, 173
Chaboyer, B., Green, E. M., & Liebert, J. 1999, AJ, 117, 1360
Chaboyer, B., Fenton, W. H., Nelan, J. E., Patnaude, D. J., & Simon, F. E. 2001, ApJ, 562, 521 (http://andes.dartmouth.edu/StellarEvol/)
Chaplin, W. J., et al. 1999, MNRAS, 308, 424
Chaplin, W. J., et al. 2010, ApJ, 713, L169
Christensen-Dalsgaard, J. 1993, ASP Conf., 42, 347
Christensen-Dalsgaard, J. 1998, Space Sci. Rev., 85, 19
Christensen-Dalsgaard, J. 2004, Sol. Phys., 220, 137
Christensen-Dalsgaard, J., et al. 2007, Communications in Asteroseismology, 150, 350
Christensen-Dalsgaard, J. 2008a, Ap&SS, 316, 13
Christensen-Dalsgaard, J. 2008b, Ap&SS, 316, 113
Cox, A. N. 2000, Allen's astrophysical quantities, 4th ed. (New York: Springer)
Deheuvels, S., & Michel, E. 2009, Ap&SS, 241, in press
Deheuvels, S., et al. 2010, a, accepted (arXiv:1003.4368)
Demarque, P., & Mengel, J. G. 1971, ApJ, 164, 317
Demarque, P., et al. 2004, ApJS, 155, 667
Demarque, P., et al. 2008, Ap&SS, 316, 311
Di Mauro, M. P., et al. 2003, A&A, 404, 341
Dotter, A., et al. 2007, AJ, 134, 376
Eggenberger, P. & Carrier, F. 2006, A&A, 449, 293
Eggenberger, P., Meynet, G., Maeder, A., et al. 2008, Ap&SS, 316, 43
Eggenberger, P., Miglio, A., Montalban, J., et al. 2010, A&A, 509, 72
Eggleton, P. P., Faulkner, J., & Flannery, B. P. 1973, A&A, 23, 325
Ferguson, J. W., et al. 2005, ApJ, 623, 585
Fernandes, J., & Monteiro, M.J.P.F.G. 2003, A&A, 399, 243
Frasca, A., et al. 2003, A&A, 405, 149
Frasca, A., et al. 2006, A&A, 454, 301
Gilliland, R. L., et al. 2010a, PASP, 122, 131
Gilliland, R. L., et al. 2010b, ApJ, 713, L160
Grevesse, N., & Noels, A. 1993, in Origin and Evolution of the Elements, ed. S. Kubono & T. Kajino, 14
Grevesse, N. & Sauval, A. J. 1998, Space Sci. Rev., 85, 161
Grevesse, N., Asplund, M., Sauval, A. J., 2007 Space Sci. Rev., 130, 105
Guenther, D. B., et al. 1992, ApJ, 387, 372
Gustafsson, et al. 2008, A&A, 486, 951
Harvey, J., 1985, ESA SP-235, 199
Hubeny, I. 1988, Comput. Phys. Comm., 52, 103
Hubeny I., Lanz T., 1995, ApJ, 439, 875
Hummer, D.G., & Mihalas, D. 1988, ApJ, 331, 794
Iglesias, C. A., & Rogers, F. J. 1996, ApJ, 464, 943
Katz, D., et al. 1998, A&A, 338, 151
Kawaler, S. D. 1988, ApJ, 333, 236
Kippenhahn, R., & Weigert, A. 1990, Stellar Structure and Evolution, (Heidelberg: Springer)
Kjeldsen, H., & Bedding, T. R. 1995, A&A, 293, 87
Kjeldsen, H., et al. 1995, AJ, 109, 1313
Kjeldsen, H., et al. 2003, AJ, 126, 1483
Kjeldsen, H., et al. 2008, ApJ, 683, L175
Kosovichev, A. G. 1999, J. Comput. App. Math., 109, 1
Kurucz, R. L. 1991, in NATO ASIC Proc. 341: Stellar Atmospheres - Beyond Classical Models, 441
Kurucz, R.L., 1993 ATLAS9 Stellar Atmosphere Programs and 2 km s^{-1} grid, (Kurucz CD-ROM No. 13)
Larson, R. B., & Demarque, P. R. 1964, ApJ, 140, 524
Latham, D. W., et al. 2005, BAAS, 37, 1340
Ludwig, H.-G. et al. 2009, IAU Symp., 265, 201
Maeder, A. & Meynet, G. 1989, A&A, 210, 155
Maeder, A. & Zahn, J.-P. 1998, A&A, 334, 1000
Metcalfe, T. S., & Charbonneau, P. 2003, J. Computat. Phys., 185, 176
Metcalfe, T. S., et al. 2009, ApJ, 699, 373
Michaud, G., & Proffitt, C. R. 1993, ASP Conf., 40, 246
Monet, D. G., et al. 2010, ApJ, submitted (arXiv:1001.0305)
Morel, P. 1997, A&AS, 124, 597
Morel P., Lebreton Y., 2008, Ap&SS, 316, 61
Moya, A. & Garrido, R. 2008, Ap&SS, 316, 129
Osaki, J. 1975, PASJ, 27, 237
Paquette, C., Pelletier, C., Fontaine, G., & Michaud, G. 1986, ApJS, 61, 177
Pinheiro, F.J.G., & Fernandes, J.M. 2010, Ap&SS, 328, 73
Quirion, P.-O., Christensen-Dalsgaard, J. & Arentoft, T. 2010, in prep.
Randich, S., et al. 2006, A&A, 450, 557
Rogers, F. J., & Iglesias, C. A. 1995, ASP Conf., 78, 31
Rogers, F.J., Swenson, F.J., & Iglesias, C.A. 1996, ApJ, 456, 902
Rogers, F. J. & Nayfonov, A. 2002, ApJ, 576, 1064
Senden C., 1973 http://verdi.as.utexas.edu/
Soderblom, D. R. 2010, ARA&A, 48, in press (arXiv:1003.6074)
Soriano, M., & Vauclair, S. 2010, A&A, 513, A49

Soubiran, C., Katz, D., & Cayrel, R. 1998, A&AS, 133, 221
Soufi, F., Goupil, M. J., & Dziembowski, W. A. 1998, A&A, 334, 911
Sousa S.G., et al. 2006, A&A, 458, 873
Sousa S.G., et al. 2007, A&A, 469, 783
Sousa S.G., et al. 2008, A&A, 487, 373
Stello, D., et al. 2009a, ApJ, 700, 1589
Stello, D., et al. 2009b, MNRAS, 400, L80
Suárez, J. C. 2002, Ph.D. Thesis, Observatoire de Paris.
Suárez, J. C., Garrido, R., & Moya, A. 2007, A&A, 474, 961
Suárez, J. C., & Goupil, M. J. 2008, Ap&SS, 316, 155
Thoul, A. A., Bahcall, J. N., & Loeb, A. 1994, ApJ, 421, 828
Vauclair, S., et al. 2008, A&A, 482, L5
Weiss, A., & Schlattl, H. 2008, Ap&SS, 316, 99
Yang, W., & Meng, X. 2010, New Astronomy, 15, 367
Zahn, J.-P. 1992, A&A, 265, 115

APPENDIX

A. THE INFLUENCE OF ROTATION

Rotation velocity can have a large influence on the frequencies of a given stellar model, since angular momentum transport can change the internal structure and evolution of the star. Thus, rotation velocity and angular momentum transport processes must be taken into account for accurate modeling. However, if the rotation velocity is not too large, the effect on the frequencies can be comparable to or smaller than the observational accuracy, in which case non-rotating models can be trusted. We have examined two angular momentum transport processes covering the extreme cases to quantify the influence of rotation on the modeling of KIC 11026764.

The study was performed using the CESAM code (Morel & Lebreton 2008). The first-order effects of rotation on the equilibrium models were considered by subtracting the spherically averaged contribution of the centrifugal acceleration to the gravity of the model, $g_{\rm eff} = g - \mathcal{A}_c(r)$, where g corresponds to the local gravity, and $\mathcal{A}_c(r)$ represents the radial component of the centrifugal acceleration. This spherically averaged component of the centrifugal acceleration does not change the order of the hydrostatic equilibrium equations. Such models are referred to as *pseudo-rotating* (see Soufi et al. 1998; Suárez et al. 2007). Since we have only a weak constraint on the rotation velocity of KIC 11026764 (see §3.2), we used an initial rotation velocity that leads to solar rotation at the solar age. Standard physical inputs were used, including the EFF equation of state. The opacity tables were taken from the OPAL package (Rogers & Iglesias 1995), complemented at low temperatures ($T \leq 10^4$ K) with the tables provided by Alexander & Ferguson (1994). The outer boundary conditions were determined by assuming a plane-parallel Eddington grey atmosphere. The model metallicity (Z/X) is derived from the observed [Fe/H] value assuming $(Z/X)_\odot = 0.0245$ (Grevesse & Noels 1993), $Y_{\rm pr} = 0.235$ and $Z_{\rm pr} = 0$ for the primordial helium and heavy-element abundances, and $\Delta Y/\Delta Z = 2$ for the enrichment ratio. The thermonuclear reactions incorporated the PP and CNO cycles with the NACRE coefficients. No microscopic diffusion was included in the calculation.

We studied the following angular momentum transport processes: (1) Global Conservation of the angular momentum [GC, solid rigid rotation]: $\Omega(t,r) = \Omega(t)$, and (2) Local Conservation of the angular momentum [LC, differential rotation]: $d\,r^2\Omega/dt = 0$. The GC and LC of angular momentum represent the two extreme cases in nature. The actual rotation profile of the star must fall between these two solutions.

The theoretical frequencies were calculated using GraCo (Moya & Garrido 2008). We found that for the rotation velocity studied here, rigid rotation yields frequencies closer to the non-rotating case, with differences in the range [−0.01, −0.025] μHz. Differential rotation yields larger differences in the range [−0.051, −0.045] μHz. Considering the large frequency separations, rigid rotation leads to differences relative to the non-rotating case in the range [+0.0025, −0.0045] μHz while differential rotation yields differences in the range [0, −0.004] μHz. All of these differences are much smaller than the observational errors, so rotation can safely be neglected in the frequency analysis of KIC 11026764. However, note that rotational mixing—which has not been considered in this study—may lead to changes in the global and internal properties of the models even for slowly rotating stars (Eggenberger et al. 2010).

B. THE IMPORTANCE OF ASTEROSEISMIC CONSTRAINTS

We compared results from SEEK with and without the asteroseismic inputs to see how the large and small separations can help reduce the uncertainty on the inferred stellar properties. We see that the uncertainty in the radius of 3% provided by SEEK is in line with what was expected from simulated data (Stello et al. 2009a). With $R = 2.10 \pm 0.06\ R_\odot$, the precision is a factor of five better than what we could get using only the available spectroscopic input ($T_{\rm eff}$, $\log g$ and [Fe/H]), which resulted in a 14.6% uncertainty ($R = 2.06 \pm 0.30\ R_\odot$). This dramatic improvement was obtained using the large and small separations as the only seismic constraints, as opposed to fitting individual mode frequencies.

In Figure 5 we show 2D projections of the probability distributions provided by SEEK, which illustrate the correlations between the spectroscopic input parameters and the value of the inferred radius. To produce these figures we fixed all but one of the spectroscopic input parameters to the observed values. Hence, in Figure 5a the dark red regions are where we would most likely find the star if we did not know its temperature. The cross marks the observed value of the temperature with its measured uncertainty in the vertical direction while the horizontal direction marks the inferred value of R and its precision. We can see that changing the temperature within the error bars does not greatly affect the value of the radius. Reducing the uncertainty of the temperature would not affect the uncertainty of the radius, since the width of the correlation function is large compared to its slope. In Figure 5b we see that the value of $\log g$ is well determined without any spectroscopic measurement. The spectroscopic value of $\log g$ has no significant influence in constraining the radius. The constraints from the seismic measurements are simply much stronger than what is found from spectroscopy in this case. We found similar results for the determination of the mass. Quite apparent in Figure 5c are several local maxima due to the discrete nature of the grid. However, the resolution of the grid is sufficient to see the underlying correlation between the metallicity and the radius. From this figure we see that if the star had a

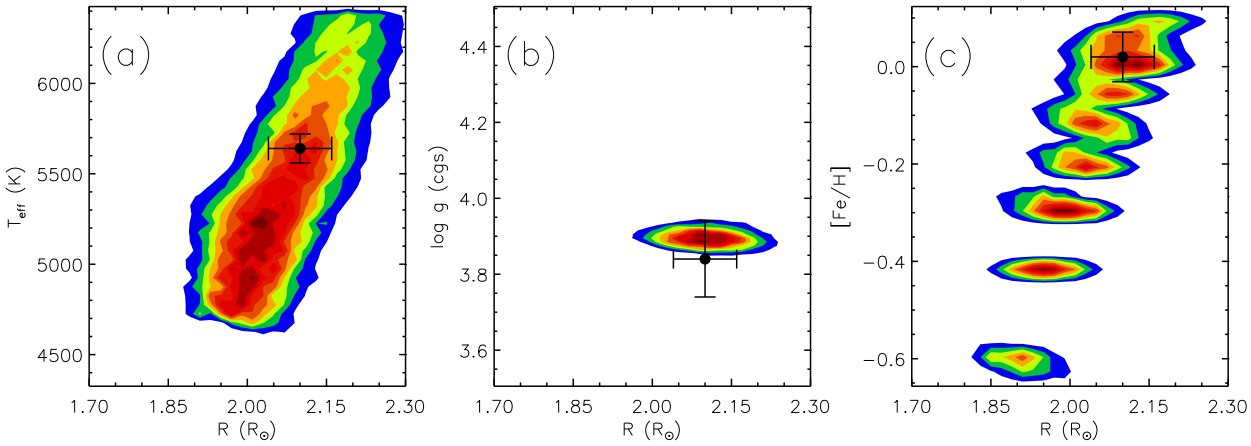

Figure 5. Normalized probability distributions, showing the correlation of the radius with several spectroscopic constraints when they are excluded from the fit, including (a) the effective temperature $T_{\rm eff}$, (b) the surface gravity $\log g$ and (c) the metallicity [Fe/H] relative to solar, where the gaps between the islands are caused by the discrete nature of the grid. Dark red indicates the maximum probability, which decreases linearly to white for zero probability. In each panel, the cross shows the observed values from the VWA method (see Table 2) and the final fit for $R = 2.10 \pm 0.06$. We see that $\log g$ is determined precisely before any spectroscopic knowledge of its value is included in the fit.

metallicity of [Fe/H] $\sim$ –0.6 it would have a radius of $R \sim 1.91\ R_\odot$. We remark that the uncertainty in radius is mainly caused by the unknown value of the initial helium content $Y_{\rm i}$ which has not been constrained by any of the observables (for more details on the effect of $Y_{\rm i}$ on stellar parameters, see Quirion, Christensen-Dalsgaard & Arentoft 2010).

Finally, in Figure 6 both the large and the small separations are left as free parameters. We note that the curved shape of the probability function is typical when the correlation between the large separation and the radius is plotted. In addition to showing that the large separation is the main constraint on the radius, Figure 6 illustrates that a star with a large radius, and hence smaller value of the large separation, will have a larger uncertainty on the inferred radius. The larger uncertainty is caused by the changing slope of the correlation, which tends to be flatter for larger radii. Figure 6 also shows that without the asteroseismic constraints, the uncertainty in the radius increases dramatically since the most probable region for the radius, in red, spans $1.76 \lesssim R/R_\odot \lesssim 2.36$.

For the mass, SEEK demonstrates that the precision is only slightly improved by including the large an small separations in the fitting process. We find $M = 1.25 \pm 0.13\ M_\odot$ when only the spectroscopic input parameters are used and $M = 1.27 \pm 0.09\ M_\odot$ when asteroseismic inputs are added. For the age, the results of SEEK without the asteroseismic inputs yield a relatively weak constraint of 40% with $t = 5.03 \pm 2.02$ Gyr. This uncertainty is reduced by nearly a factor of two when the large and small separations are used, which gives $t = 4.26 \pm 1.22$ Gyr. If we compare this result with Quirion, Christensen-Dalsgaard & Arentoft (2010), 30% error on the age is unusually large for a star having well measured values of $\Delta\nu$ and $\delta\nu$. It seems that $\delta\nu$ does not provide an additional constraint on the age of the star, since we were able to determine a very similar age $t = 4.21 \pm 1.25$ Gyr when $\delta\nu$ was excluded from the fit. Bedding et al. (in prep.) find this to be generally true for subgiant stars.

Finally, we stress that the mixing-length parameter α and the initial helium content $Y_{\rm i}$ are not constrained by our fit. For $Y_{\rm i}$, the output value is simply the central value used in SEEK's grid plus a 1σ uncertainty extending toward the edges of the grid. For α, a value smaller than 1.8 is preferred, but not decisively. Our overall conclusion from SEEK is that the asymptotic asteroseismic inputs can be used to reduce significantly the uncertainty on the radius of KIC 11026764. The age and the mass precision can also be improved, though less substantially.

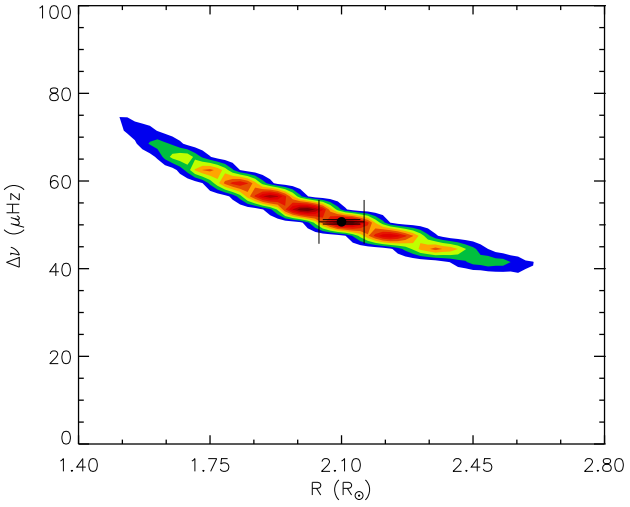

Figure 6. Similar to Figure 5, but for $\Delta\nu_0$ when the small separation is also excluded from the fit. The point with error bars indicates the result when both the large and small separations are included as constraints.